A NEW STAR FORMATION RATE CALIBRATION FROM POLYCYCLIC AROMATIC HYDROCARBON EMISSION FEATURES AND APPLICATION TO HIGH-REDSHIFT GALAXIES

Heath V. Shipley[1,2], Casey Papovich[1], George H. Rieke[3], Michael J. I. Brown[4], and John Moustakas[5]

[1] George P. and Cynthia Woods Mitchell Institute for Fundamental Physics and Astronomy, and Department of Physics & Astronomy, Texas A&M University, College Station, TX 77843-4242, USA

[2] Department of Physics & Astronomy, Tufts University, 574 Boston Avenue Suites 304, Medford, MA 02155, USA; heath.shipley@tufts.edu

[3] Steward Observatory, University of Arizona, 933 North Cherry Avenue, Tucson, AZ 85719, USA

[4] School of Physics & Astronomy, Monash University, Clayton, Victoria 3800, Australia

[5] Department of Physics & Astronomy, Siena College, Loudonville, NY 12211, USA

ABSTRACT

We calibrate the integrated luminosity from the polycyclic aromatic hydrocarbon (PAH) features at 6.2, 7.7, and 11.3 μm in galaxies as a measure of the star formation rate (SFR). These features are strong (containing as much as 5%–10% of the total infrared luminosity) and suffer minimal extinction. Our calibration uses *Spitzer* Infrared Spectrograph (IRS) measurements of 105 galaxies at $0 < z < 0.4$, infrared (IR) luminosities of 10^9–10^{12} $L_\odot$, combined with other well-calibrated SFR indicators. The PAH luminosity correlates linearly with the SFR as measured by the extinction-corrected Hα luminosity over the range of luminosities in our calibration sample. The scatter is 0.14 dex, comparable to that between SFRs derived from the Paα and extinction-corrected Hα emission lines, implying that the PAH features may be as accurate an SFR indicator as hydrogen recombination lines. The PAH SFR relation depends on gas-phase metallicity, for which we supply an empirical correction for galaxies with $0.2 Z_\odot < Z \lesssim 0.7 Z_\odot$. We present a case study in advance of the *James Webb Space Telescope* (*JWST*), which will be capable of measuring SFRs from PAHs in distant galaxies at the peak of the SFR density in the universe ($z \sim 2$) with SFRs as low as $\sim$10 $M_\odot$ yr^{-1}. We use *Spitzer*/IRS observations of the PAH features and Paα emission plus Hα measurements in lensed star-forming galaxies at $1 < z < 3$ to demonstrate the ability of the PAHs to derive accurate SFRs. We also demonstrate that because the PAH features dominate the mid-IR fluxes, broadband mid-IR photometric measurements from *JWST* will both trace the SFR and provide a way to exclude galaxies dominated by an active galactic nucleus.

Key words: galaxies: active – galaxies: evolution – galaxies: high-redshift – infrared: galaxies

1. INTRODUCTION

Star formation is a fundamental property of galaxy formation and evolution. Understanding the exact rate of star formation and how it evolves with time and galaxy mass has deep implications for how galaxies form. Measuring accurate star formation rates (SFRs) through cosmic time is therefore paramount for understanding galaxy evolution itself. Much work has been applied to calibrating emission from the UV, nebular emission lines, far-IR, X-ray, and radio as tracers of the SFR in distant galaxies (see the review by Kennicutt & Evans 2012).

The epoch $1 < z < 3$ is particularly interesting as it corresponds to the peak cosmic SFR density in the universe (Madau & Dickinson 2014, and references therein). There are different measures of the instantaneous SFR (see, e.g., Kennicutt 1998), which are useful for probing the SFR density evolution, but their utility depends on the redshift of the source and observational wavelengths available. At low redshifts in this range, [O II] λ3727 is frequently used to measure SFRs, but it is subject to large extinction corrections (Kennicutt 1998) and hence large uncertainties. Although the [O II] line should be excited by star formation, for galaxies with strong active galactic nuclei (AGNs) such as quasars, their spectra generally show no [O II] emission beyond that expected from the AGN (Ho 2005), i.e., the quasar dominates the excitation and the line cannot be used to probe the host galaxies. UV continuum emission is a more general probe, but it is also subject to extinction and to ambiguities of interpretation in galaxies with AGNs. Rest-frame optical lines (e.g., Hα) shifted into the near-IR are observationally expensive and also suffer from ambiguities if there is an AGN.

Deep IR surveys with *ISO*, *Spitzer*, and *Herschel* have proven to be a powerful tool to explore SFRs across this range and have revealed that the majority of star formation at redshifts of $z \sim 1$–3 occurs in dust-enshrouded galaxies (e.g., Elbaz et al. 2011; Murphy et al. 2011), and that luminous IR galaxies (LIRGs, $L_{\rm IR} = 10^{11}$–10^{12} $L_\odot$) and ultraluminous IR galaxies (ULIRGs, $L_{\rm IR} > 10^{12}$ $L_\odot$) are much more prevalent during these earlier epochs than today (Chary & Elbaz 2001; Le Floc'h et al. 2005; Pérez-González et al. 2005; Magnelli et al. 2009; Elbaz et al. 2011; Murphy et al. 2011; Lutz 2014, and references therein). Not only do far-IR measurements reveal dust-obscured star formation, but even in luminous quasars, this emission appears to be dominated by the power from star formation in the host galaxies (Rosario et al. 2013; Xu et al. 2015). The Atacama Large Millimeter Array (ALMA) can measure rest-frame far-IR outputs for $z \gtrsim 2$, but at lower redshifts it becomes inefficient in this application. Furthermore, no far-IR missions are planned for the immediate future, making it difficult to extend this method past the results from *Spitzer* and *Herschel*. The *James Webb Space Telescope* (*JWST*) is a promising approach for $z \lesssim 2$ if accurate SFRs can be derived from observations at rest wavelengths of $\sim$8 μm (e.g., Rujopakarn et al. 2013).

It has been argued that estimation of SFRs using the aromatic emission features[6] that dominate the 8 μm emission of star-forming galaxies is subject to substantial scatter (e.g., Smith et al. 2007; Bendo et al. 2008). However, these features do track the total SFR at some level, and if they could be calibrated accurately, they would have numerous advantages. For example, *Spitzer* 24 μm measurements provide perhaps the deepest probe available of SFRs for $1 < z < 3$ (Elbaz et al. 2011). The luminosity in the mid-IR PAH emission bands is very high for galaxies with ongoing star formation. The total PAH emission can contribute as much as 20% of the total IR luminosity, and the 7.7 μm PAH band may contribute as much as 50% of the total PAH emission (e.g., Smith et al. 2007; Wu et al. 2010; Shipley et al. 2013). In addition, for galaxies with an AGN the PAH features have been shown to trace the SFR from the integrated light of the galaxy (if the AGN is not the dominant source of the integrated light; e.g., Shipley et al. 2013). Furthermore, the 11.3 μm PAH feature even in the immediate vicinity of an AGN is not significantly suppressed (Diamond-Stanic & Rieke 2010).

Interpreting existing deep *Spitzer* and future *JWST* measurements of embedded star formation depends on developing confidence in the use of the PAH features for this purpose. In this paper, we therefore discuss the utility of using the PAH emission to study the SFR in galaxies over a large range of total IR luminosity and metallicity to determine a robust calibration of the relation between PAH emission and the SFR. There are previous efforts that calibrate the PAH emission as an SFR indicator. Some of these works focus on high-luminosity objects and calibrate against the total IR luminosity, where for these objects there may be unknown contributions to the emission from AGN and/or unknown optical depth effects (Lutz et al. 2008; Pope et al. 2008; Fu & Stockton 2009). Other studies have focused on the broadband emission in the mid-IR, which contains contributions from both the continuum and PAH emission (Calzetti et al. 2007; Fumagalli et al. 2014; Battisti et al. 2015). There is a need for a PAH SFR indicator calibrated over a range of bolometric luminosity using the luminosity in the PAH emission features themselves. Once this has been accomplished, it is also possible to understand and improve measurements of SFRs based on photometry in the 8 μm region.

This paper presents one of the first efforts to calibrate the PAH emission itself against robust SFR measures of the integrated light for distant galaxies over a large range of total IR luminosity (Section 5). To do so, we take advantage of PAH emission feature measurements using a sample of galaxies with *Spitzer*/IRS spectroscopy out to $z < 0.4$. The outline for the paper is as follows. In Section 2, we define our main calibration sample and describe a high-redshift demonstration sample. In Section 3, we describe our analysis of the derived quantities. In Section 4, we present our SFR relations in terms of the PAH luminosity. In Section 5, we discuss previous calibrations of the PAH luminosity as an SFR indicator. In Section 6, we demonstrate our PAH SFR relations with the demonstration sample of high-redshift lensed galaxies. In Section 7, we present our conclusions. The ΛCDM cosmology we assume is $H_0 = 70$ km s^{-1} Mpc^{-1}, $\Omega_m = 0.3$, and $\Omega_\lambda = 0.7$ throughout

this work (previous studies we reference throughout this work predominantly use this cosmology, and we adopt it as well to be consistent as much as possible). We adopt a Kroupa initial mass function (IMF) throughout this work, where the IMF has the slope $\alpha = 2.3$ for stellar masses 0.5–100 $M_\odot$ and a shallower slope $\alpha = 1.3$ for the mass range 0.1–0.5 $M_\odot$. The Kroupa IMF is consistent with observations of the Galactic field IMF (e.g., Chabrier 2003; Kroupa & Weidner 2003).

2. SAMPLE AND DATA

2.1. Calibration Sample

For proper calibration of the PAH features as an SFR indicator, we carefully selected galaxies that had full coverage of the *Spitzer*/IRS spectrum and *Spitzer*/MIPS 24 μm observations. We required the galaxies in our sample to have complete optical coverage of the important emission lines needed (specifically Hβ, [O III] λ5007, Hα, and [N II] λ6583) to measure extinction-corrected SFRs from the Hα emission line luminosity (Kennicutt et al. 2009) and to estimate the ionization state (Kewley et al. 2001; Kauffmann et al. 2003) and the gas-phase metallicity (Pettini & Pagel 2004). We also required that the galaxies be sufficiently distant that the *Spitzer*/IRS contains the majority of the integrated light in the spectroscopic slit. In effect, this limits us to $z > 0.01$ or where robust aperture corrections are available. Aperture corrections for each sample were performed in the same general way. Photometry for the integrated light of the galaxy was obtained and used to estimate the correction factors applied to the optical and IR spectra from the smaller aperture sizes used for the spectral slits (see below for more details).

We identified three galaxy samples from the literature that fulfill our selection criteria. We use these three samples as our Calibration Sample to establish the PAH luminosity as an SFR indicator. The calibration sample includes a broad range of galaxies allowing for a robust calibration of the PAH luminosity for vastly different systems. The full calibration sample includes 286 galaxies with data from O'Dowd et al. (2009), Shipley et al. (2013), and Brown et al. (2014) samples (specific steps taken for data reduction of the spectra can be found therein). We discuss each sample briefly in the following sections. Optical and IR aperture corrections were performed by both O'Dowd et al. (2009) and Brown et al. (2014) and can be found therein. For Shipley et al. (2013), IR aperture corrections were performed and can be found in the reference. Optical aperture corrections were on average ~10% for the Shipley et al. (2013) sample for the optical line fluxes shown in Table 1. A few sources from Brown et al. (2014) are below our redshift requirement of $z > 0.01$. We keep these galaxies in our primary and secondary calibration samples because Brown et al. (2014) achieved very accurate aperture corrections to construct their spectral energy distributions (SEDs), but this may introduce some bias for a few galaxies as the aperture corrections may not apply equally between the nuclear regions used for spectroscopy and the galaxy outskirts.

We excluded from our full calibration sample those objects with poor data quality, where measured line/feature fluxes are upper limits in one or more of the required emission features: Hα, the three brightest PAH features (6.2, 7.7, and 11.3 μm features), or the MIPS 24 μm band. Also, other reasons made it necessary to exclude galaxies from the full calibration sample: not all galaxies in Brown et al. (2014) have *Spitzer* IRS

---

[6] Lying in the range 3–19 μm, attributed to polycyclic aromatic hydrocarbons and termed "PAH" hereafter. Certain PAH bands are made up of several emission features (e.g., 7.7, 8.6, 11.3, 12.7, and 17.0 μm PAH bands), and so we will use the general term "feature" to describe the PAH emission bands.

Table 1
Optical Fluxes and BPT Classification for Shipley et al. (2013) Sample

ID	$H\beta$ (10^{-16})	[O III] $\lambda5007$ (10^{-16})	$H\alpha$ (10^{-16})	[N II] $\lambda6583$ (10^{-16})	BPT Class
1	22.4 ± 0.33	41.8 ± 0.32	89.6 ± 0.44	16.0 ± 0.27	SF
2	…	…	…	…	…
3	0.99 ± 0.34	…	…	…	…
4	9.88 ± 0.30	1.22 ± 0.20	63.2 ± 0.37	21.9 ± 0.28	SF
5	60.5 ± 1.18	18.6 ± 1.00	$414. \pm 2.29$	$155. \pm 1.79$	SF
6	1.70 ± 0.30	1.49 ± 0.32	11.9 ± 0.51	7.40 ± 0.47	SF/AGN
7	51.7 ± 0.43	10.7 ± 0.33	$258. \pm 1.56$	98.9 ± 0.62	SF
8	1.83 ± 0.30	1.78 ± 0.26	13.8 ± 0.39	13.8 ± 0.35	AGN
9	0.56 ± 0.12	0.49 ± 0.10	4.32 ± 0.20	3.32 ± 0.19	SF/AGN
10	2.92 ± 0.24	2.38 ± 0.22	22.4 ± 0.51	12.7 ± 0.50	SF/AGN
11	0.36 ± 0.09	0.24 ± 0.12	1.32 ± 0.24	…	…
12	6.93 ± 0.26	7.52 ± 0.28	40.9 ± 0.75	17.0 ± 0.64	SF/AGN
13	…	…	…	…	…
14	0.82 ± 0.28	…	4.33 ± 0.76	2.64 ± 0.49	…
15	10.0 ± 0.26	5.75 ± 0.25	65.6 ± 1.00	29.4 ± 0.77	SF
16	…	1.36 ± 0.27	…	…	…
17	4.52 ± 0.17	3.37 ± 0.16	38.0 ± 0.50	17.5 ± 0.39	SF/AGN
18	21.7 ± 0.35	12.4 ± 0.34	$120. \pm 0.72$	42.6 ± 0.59	SF
19	2.14 ± 0.13	3.42 ± 0.09	11.0 ± 0.36	2.57 ± 0.27	SF
20	2.42 ± 0.20	0.69 ± 0.18	14.4 ± 0.41	7.04 ± 0.44	SF
21	1.51 ± 0.24	8.42 ± 0.25	7.22 ± 0.62	5.65 ± 0.60	AGN
22	7.71 ± 0.35	13.9 ± 0.37	39.3 ± 1.65	25.4 ± 1.16	SF/AGN
23	10.4 ± 0.75	4.74 ± 0.65	75.6 ± 2.34	30.5 ± 2.04	SF
24	0.94 ± 0.26	12.3 ± 0.24	…	…	…
25	5.66 ± 0.38	4.95 ± 0.40	28.1 ± 1.10	18.1 ± 1.19	SF/AGN
26	…	4.77 ± 0.42	…	…	…
27	1.46 ± 0.25	4.45 ± 0.27	7.11 ± 1.15	6.72 ± 0.95	AGN
28	3.43 ± 0.13	1.66 ± 0.15	22.5 ± 0.82	6.31 ± 0.71	SF
29	2.01 ± 0.28	5.83 ± 0.31	…	…	…
30	2.42 ± 0.24	2.01 ± 0.18	…	…	…
31	4.92 ± 0.21	1.83 ± 0.16	…	…	…
32	1.76 ± 0.10	0.58 ± 0.10	…	…	…
33	1.21 ± 0.29	…	7.17 ± 0.64	2.78 ± 0.44	…
34	1.81 ± 0.14	0.92 ± 0.11	…	…	…
35	2.00 ± 0.47	…	…	…	…
36	1.01 ± 0.16	…	…	…	…
37	0.47 ± 0.08	1.53 ± 0.09	2.97 ± 0.29	1.67 ± 0.19	AGN
38	…	0.81 ± 0.13	…	…	…
39	…	…	…	…	…
40	0.51 ± 0.14	…	6.08 ± 0.62	5.79 ± 0.54	…
41	…	0.71 ± 0.20	3.08 ± 0.33	5.53 ± 0.36	…
42	1.16 ± 0.19	1.27 ± 0.21	10.3 ± 0.81	9.67 ± 0.73	AGN
43	…	…	…	…	…
44	1.58 ± 0.27	9.40 ± 0.34	…	…	…
45	1.22 ± 0.22	2.93 ± 0.26	…	…	…
46	2.75 ± 0.26	3.15 ± 0.20	12.1 ± 0.32	2.55 ± 0.21	SF
47	7.01 ± 0.29	3.68 ± 0.22	40.5 ± 0.51	14.9 ± 0.55	SF
48	5.45 ± 0.17	1.62 ± 0.19	59.2 ± 2.79	26.0 ± 2.99	SF
49	4.16 ± 0.71	18.0 ± 1.29	20.9 ± 4.05	13.4 ± 4.39	AGN
50	…	…	…	…	…

Note. Column (1) is the galaxy identification defined in Shipley et al. (2013). Columns (2)−(5) are the measured fluxes for the emission lines $H\beta$, [O III] $\lambda5007$, $H\alpha$, and [N II] $\lambda6583$, respectively (in units of erg s^{-1} cm^{-2}). Column (6) is the BPT classification from the measured fluxes.

coverage (resulting from passive galaxies without significant mid-IR dust emission); the sources in the *Spitzer* First Look Survey (FLS) from Shipley et al. (2013) do not have optical spectroscopy covering $H\alpha$. We discuss these reasons in detail in the following sections for each sample. This reduced our calibration sample to 227 galaxies.

Finally, we restricted our calibration sample to include only star-forming galaxies with no indications of AGNs (which can contribute to both the $H\alpha$ and 24 μm emission), and we required all galaxies to have approximately solar gas-phase metallicity (see Section 3.4 below). These restrictions reduced our calibration sample to 105 galaxies fitting all the requirements. This constitutes our Primary Calibration Sample. In what follows, we focus the PAH SFR calibration on this primary calibration sample of 105 galaxies, which span redshift $0.0 < z < 0.4$ and IR luminosity $10^9 < L_{IR}/L_\odot < 10^{12}$. We

also consider a secondary calibration sample of 25 galaxies that satisfy all our selection criteria but have subsolar metallicity (see Sections 3.4 and 4.3).

2.1.1. O'Dowd et al. (2009) Sample

The O'Dowd et al. (2009) sample consists of 92 galaxies that cover a range in total IR luminosity of $L_{IR} = 10^9–10^{11} \, L_{\odot}$ that complements the lower-luminosity galaxies in Brown et al. (2014) with a redshift of $0.03 < z < 0.22$ and varying AGN activity (from starbursts to AGNs). Compared to the solar oxygen abundance, $12 + \log(O/H) = 8.69$ (Asplund et al. 2009), the galaxies in the O'Dowd et al. (2009) sample span a narrow range around solar $(12 + \log(O/H)_{N2} = 8.6–8.8$ with one galaxy at 9.0). This sample has complete coverage of the optical spectra (using the emission line fluxes from the SDSS DR7), IRS spectra, and MIPS 24 μm photometry taken from the published data. Sixty-three galaxies from this sample fit our primary calibration sample criteria. Zero galaxies fit the secondary calibration sample criteria.

2.1.2. Shipley et al. (2013) Sample

The Shipley et al. (2013) sample consists of 65 galaxies covering a range in total IR luminosity of $L_{IR} = 10^{10}–10^{12} \, L_{\odot}$ with mostly higher IR luminosity compared to the Brown et al. (2014) and O'Dowd et al. (2009) samples. The sample has a redshift of $0.02 < z < 0.6$ with varying AGN activity (from domination by starbursts to AGNs). Compared to the solar oxygen abundance, the galaxies in the Shipley et al. (2013) sample span a range around solar $(12 + \log(O/H)_{N2} = 8.4–8.8$ but have metallicities that bridge the other two samples. This sample has complete IR coverage of the IRS and MIPS 24 μm photometry and complete optical spectroscopic data for 26 of the galaxies in the sample. Twelve galaxies from this sample fit our primary calibration sample criteria. Two galaxies fit the secondary calibration sample criteria.

2.1.3. Brown et al. (2014) Sample

The Brown et al. (2014) study included 129 galaxies, covering a large range in total IR luminosity $(L_{IR} = 10^9–10^{12} \, L_{\odot})$ and a diverse range in morphology (from dwarf irregulars to ellipticals) with a redshift of $0.0 < z < 0.06$ and varying AGN activity (from starbursts to AGNs), and is largely drawn from the integrated optical spectroscopic samples of Moustakas & Kennicutt (2006) and Moustakas et al. (2010). Because of the lower redshift and mostly lower IR luminosity range of the Brown et al. (2014) sample, it contains lower-metallicity galaxies $(7.8 < 12 + \log(O/H)_{N2} < 8.8)$ compared to the O'Dowd et al. (2009) and Shipley et al. (2013) samples. The Brown et al. (2014) sample also includes clearly merging systems. This extends the study of the PAH emission as an SFR indicator over a range of activity and metallicity. This sample has complete optical spectra and MIPS 24 μm photometry coverage and includes IRS spectra for 111 of the galaxies that come from several surveys (see Brown et al. 2014, and references therein; galaxies without IRS spectra are passive). We use these for our calibration sample. Thirty galaxies from this sample fit our primary calibration sample criteria. Twenty-three galaxies fit the secondary calibration sample criteria.

Because the redshift distribution of the Brown et al. (2014) sample is lower compared to the other data sets used in the calibration sample, the aperture corrections for light lost

outside the slit can be higher. Brown et al. (2014) provided aperture corrections at 8 and 12 μm, and caution must be applied when these differ significantly. For the Brown et al. (2014) galaxies in our primary calibration sample, most (23/30 galaxies) have 8 and 12 μm aperture corrections consistent with the overall sample (the aperture corrections are $\sim$1.37 and $\sim$1.34 for 8 μm and 12 μm, respectively). The remaining seven galaxies have larger differences (the aperture corrections are $\sim$2.52 and $\sim$2.35 for 8 μm and 12 μm, respectively), but a visual inspection of the spectra shows no obvious discontinuities, and none of our results would change if we exclude these galaxies.

2.2. Demonstration Sample of High-redshift Galaxies

To demonstrate the PAH SFR calibration, we use *Spitzer*/IRS data for a sample of high-redshift $(1 < z < 3)$ galaxies that have been gravitationally lensed by foreground massive galaxies and/or galaxy clusters. In many cases the gravitational lensing is substantial, boosting the flux from the background galaxies by factors of $\mu \simeq 3–30$. Because of the lensing factors, the sensitivity is what can be expected for "typical" distant galaxies observed with the *JWST* Mid-IR Instrument (MIRI). *JWST*/MIRI will be able to observe the 6.2 and 7.7 μm PAH features for galaxies with SFRs as low as $\sim$10 $M_{\odot}$ yr^{-1} to $z \lesssim 2$ by covering a wavelength range from 4.9 to 28.8 μm with greater sensitivity than any previous IR mission.[7]

We use the sample and results reported in Rujopakarn et al. (2012), which include line flux measurements (or limits) for Hα, Paα, or Brα and the PAH features. The Paα and Brα emission lines are "gold standard" SFR indicators as they trace the ionization from the same star-forming populations as Hα, but Paα and Brα suffer substantially less extinction owing to their longer wavelengths in the rest-frame near-IR. Another excellent extinction-free SFR indicator is Hα+24 μm (Kennicutt et al. 2009); Rujopakarn et al. (2012) provide this metric based on rest-frame 24 μm fluxes estimated from SED template fitting. In addition, we reprocess the *Spitzer*/IRS data for the 8 o'clock arc as Rujopakarn et al. (2012) did not report measurements for the PAH features in the mid-IR spectroscopy for this galaxy. We used their values for the redshift and lensing magnification for each galaxy (and references therein), including the 8 o'clock arc to be consistent for the sample.[8] We define these seven high-redshift lensed galaxies from Rujopakarn et al. (2012) as our demonstration sample.

We focus our comparison of the estimated PAH SFRs to the estimated Paα and Hα+24 μm SFRs in our demonstration of the PAH SFR calibration (see Section 6.2). Depending on the redshift and *Spitzer*/IRS channels observed, only one of these SFR indicators was available for each galaxy. In general, Hα+24 μm is available for the entire sample and Paα is available for $z > 2$ galaxies, where the rest-frame 24 μm fluxes come from longer-wavelength MIPS (and in some cases *Herschel*) data, or extrapolations from observed 24 μm data. The galaxies with measured Hα+24 μm fluxes only are A2218b (Rigby et al. 2008, at $z = 1.034$ and $\mu = 6.1$) and A2667a (Rigby et al. 2008, at $z = 1.035$ and $\mu = 17$). The galaxies with

---

[7]　See: http://ircamera.as.arizona.edu/MIRI/performance.htm

[8]　The approximate magnification of a lensed galaxy introduces a large uncertainty in the estimated SFR as the actual magnification may differ by a factor of a few from that of the measured. As a result, other studies may use a different magnification, which can cause the estimated SFRs to be over- or underestimated in comparison to ours.
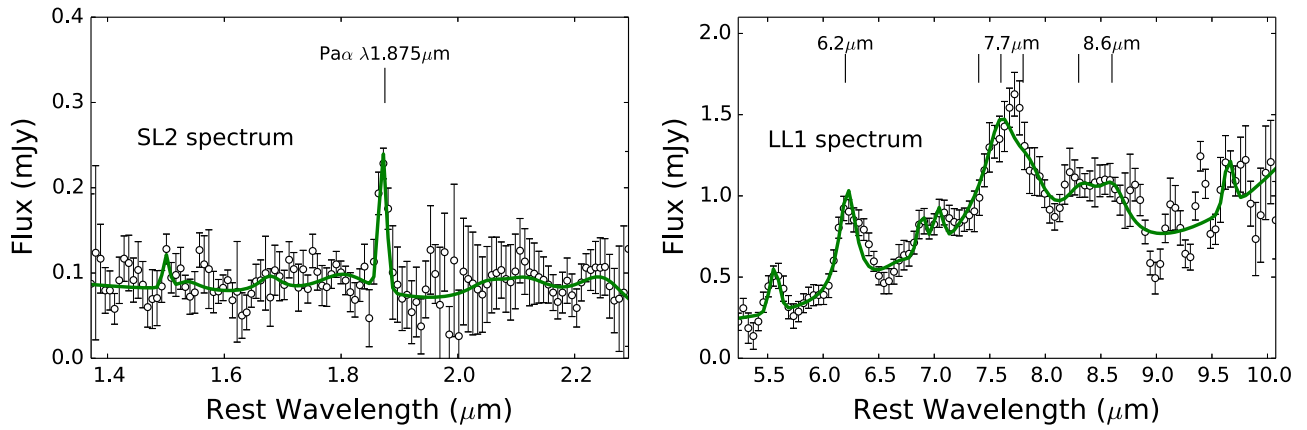
Figure 1. IRS spectra of the strongly gravitationally lensed galaxy, the "8 oclock arc." The left panel shows the SL2 spectrum, and the right panel shows the LL1 spectrum. In each panel, the data points and error bars show the measurements from the data, and the green curve shows the spectral decomposition from the best-fit PAHFIT model to the data.

measured $H\alpha+24 \mu m$ and $Pa\alpha$ fluxes are the Clone (Hainline et al. 2009; Lin et al. 2009, at $z = 2.003$ and $\mu = 27 \pm 1$), A2218a (Rigby et al. 2008; Papovich et al. 2009; Finkelstein et al. 2011, at $z = 2.520$ and $\mu = 22 \pm 2$), A1835a (Smail et al. 2005; Rigby et al. 2008, at $z = 2.566$ and $\mu = 3.5 \pm 0.5$), cB58 (Seitz et al. 1998; Teplitz et al. 2000, at $z = 2.729$ and $\mu \sim 30$), and the 8 o'clock arc (Allam et al. 2007; Finkelstein et al. 2009, at $z = 2.731$ and $\mu \sim 8$).

For the 8 o'clock arc, we reprocessed *Spitzer* data taken from program 40443 (PI: C. Papovich). We reduced the spectroscopic data for this galaxy using the S17.2.0 version of the processing software from the basic calibrated data (BCD) for the IRS SL2 and LL1 modules by following the *Spitzer* Data Analysis Cookbook, Recipe 17.[9] As in Rujopakarn et al. (2012), we were able to deblend the flux by performing point-spread function photometry to measure the flux of the arc. We reduced the IRAC and MIPS $24 \mu m$ data using the S16.1.0 version of the processing software from the BCD images by following the data reduction steps outlined in Papovich et al. (2009). We used three apertures of $1\overset{\prime\prime}{.}8$ each centered on the three components identified by Finkelstein et al. (2009) using the *Spitzer* APEX source extraction software to extract the IRAC flux from the $5.8 \mu m$ band. We estimate that the aperture corrections are 30%–50%,[10] with the contamination from a nearby LIRG at the 30%–50% level, and the corrections roughly cancel each other.

To calibrate the absolute flux density of the IRS spectra for the 8 o'clock arc, we integrated the spectrum from the SL2 module with the IRAC $5.8 \mu m$ transmission function and the spectrum from the LL1 module with the MIPS $24 \mu m$ transmission function. We took the ratio of the observed flux densities as measured directly from the IRAC and MIPS observations to the flux densities synthesized from the IRS spectra as an aperture correction. We did this to account for contamination from a foreground LIRG or light that is lost outside the spectroscopic slits. Figure 1 shows the extracted, flux-calibrated IRS SL2 and LL1 spectra for the 8 o'clock arc. We use these flux-corrected spectra to measure the $Pa\alpha$ emission line from the IRS/SL2 spectrum and the PAH

features from the IRS/LL1 spectrum. We extracted line fluxes from the IRS data for the 8 o'clock arc and the galaxies in our calibration sample using the methods described in Section 3.1.

3. DERIVED QUANTITIES

3.1. IRS Spectral Fitting

To determine flux estimates for the PAH features in the IRS spectra of our calibration sample, we used the PAHFIT spectral decomposition code (Smith et al. 2007), designed for *Spitzer* IRS data. PAHFIT uses a χ^2 minimization routine to fit a nonnegative combination of multiple emission features and continua to the one-dimensional spectra of our sources. The features included in PAHFIT are the dust emission features from PAHs (modeled as Drude profiles), thermal dust continuum, continuum from starlight, atomic and molecular emission lines (modeled as Gaussians), and dust extinction. The PAH emission features (at, e.g., 7.7, 11.3, and $17 \mu m$) are blends of multiple components, but PAHFIT treats them as individual complexes.

We take the published PAH fluxes from O'Dowd et al. (2009) and Shipley et al. (2013), which used the same PAHFIT input parameters as we use here for the Brown et al. (2014) sample (see references for specific parameters used). We fit the features in the IRS spectrum for each galaxy in Brown et al. (2014) that had an IRS spectrum (111/129 galaxies).

For the demonstration sample, the published values for the *Spitzer*/IRS spectra were fit using PAHFIT with the same parameters as our calibration sample. We use these flux measurements of $Pa\alpha$, $H\alpha+24 \mu m$, and the PAH features to estimate the SFRs.

We fit the 8 o'clock arc spectra with the same procedure. It was important to have the flux measurement fit the same way for each sample to have an accurate comparison between our PAH SFRs and the SFR indicators ($Pa\alpha$ and $H\alpha+24 \mu m$) available in Rujopakarn et al. (2012). Our measured flux values for the 8 o'clock arc are $L_{Pa\alpha} = (7.4 \pm 0.8) \times 10^{-16} \mathrm{erg\ s^{-1}\ cm^{-2}}$, $L_{6.2 \mu m} = (21.1 \pm 1.4) \times 10^{-15} \mathrm{erg\ s^{-1}\ cm^{-2}}$, and $L_{7.7 \mu m} = (80.0 \pm 11.2) \times 10^{-15} \mathrm{erg\ s^{-1}\ cm^{-2}}$. But as suggested in Rujopakarn et al. (2012), the resulting spectrum (for the LL1) has a signal-to-noise ratio (S/N) too low for PAHFIT to fit accurately the continuum and emission features owing to the contamination of the nearby sources. We do see this to some extent as PAHFIT failed to converge and yield a

---

[9] See http://irsa.ipac.caltech.edu/data/SPITZER/docs/dataanalysistools/cookbook/23/.
[10] See http://irsa.ipac.caltech.edu/data/SPITZER/docs/irac/iracinstrumenthandbook/.

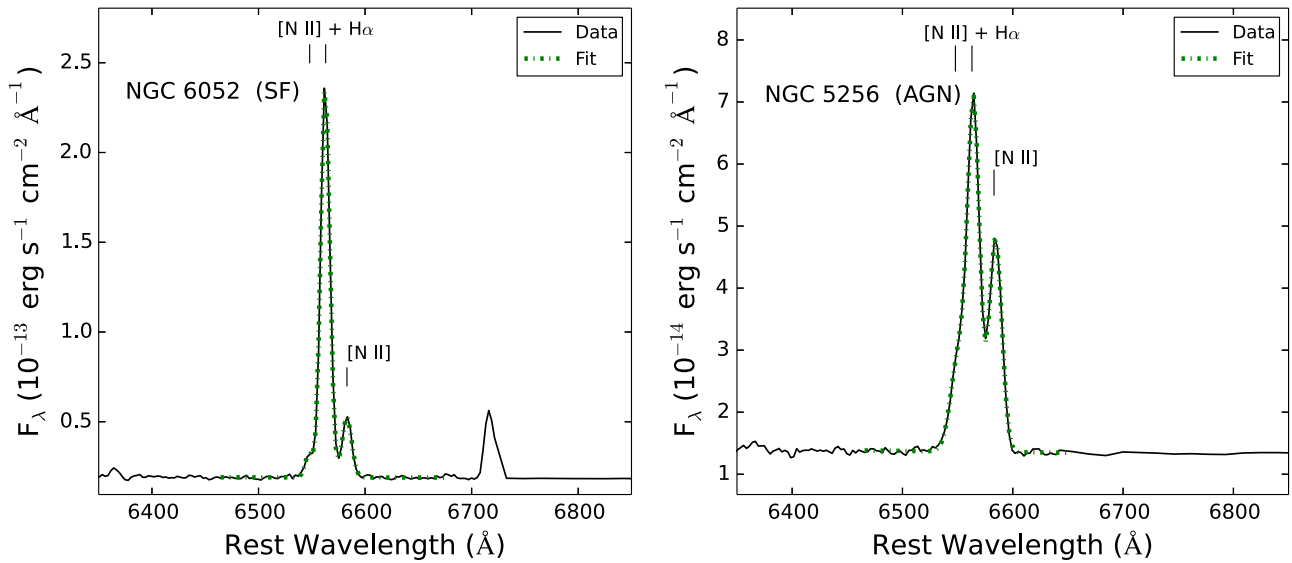**Figure 2.** Examples of our fits (green dot-dashed line) to the optical spectra (solid black line) for Brown et al. (2014) for the Hα and [N II] emission lines (see Section 3.2 for fitting procedure). Here we show NGC 6052 (star-forming) and NGC 5256 (AGN), which are representative of the entire Brown et al. (2014) sample for each classification (see Section 3.2 for classification).

more accurate fit to the PAH features in the *Spitzer*/IRS LL1 spectrum (Figure 1). Because of the galaxy's high redshift, $z = 2.731$, not all PAH features are accessible, but the 6.2 μm feature indicates an SFR = 302 ± 20.0 $M_\odot$ yr^{-1} and the 7.7 μm feature indicates an SFR = 262 ± 36.7 $M_\odot$ yr^{-1}. In contrast, the *Spitzer*/IRS SL2 spectrum gives a consistent SFR from Paα, SFR = 265 ± 29.6 $M_\odot$ yr^{-1}.

3.2. Optical Spectral Fitting

For the O'Dowd et al. (2009) sample, we used the updated line flux measurements (Hβ, [O III] λ5007, Hα, and [N II] λ6583) from SDSS DR7 (MPA/JHU value-added galaxy catalog; Brinchmann et al. 2004; Tremonti et al. 2004).[11] For Shipley et al. (2013), we used the line flux measurements from the AGN Galaxy Evolution Survey (AGES; Kochanek et al. 2012), reported in Table 1 and described in Moustakas et al. (2011) based on the continuum and emission-line fitting technique of Moustakas et al. (2010). For Brown et al. (2014), we fit the emission lines as simple Gaussians using a least-squares routine to obtain the best fit. We fit the Hα and [N II] doublet simultaneously using three Gaussians, with the ratio of the central wavelengths fixed. Figure 2 shows representative spectra and our fits for a star-forming galaxy and AGN in the Brown et al. (2014) sample.

The relationship between the [N II] λ6583/Hα and [O III] λ5007/Hβ emission line ratios provides a test for ionization from a central AGN using an optical Baldwin, Phillips, and Terlevich (BPT) classification (Kewley et al. 2001; Kauffmann et al. 2003). We adopted the SDSS DR7 measured emission line fluxes for the O'Dowd et al. (2009) sample. We note that a few of the galaxy classifications are changed from those in O'Dowd et al. (2009), which used the SDSS DR4 flux measurements. For the Shipley et al. (2013) sample, we used the measured fluxes in Table 1 for classification. For the Brown et al. (2014) sample, we use their reported optical BPT classifications.

3.3. Extinction-corrected Hα Emission Using Rest-frame MIPS 24 μm Flux

We estimate extinction-corrected Hα line luminosities using the sum of the observed Hα emission line and a fraction of the rest 24 μm monochromatic luminosity as defined by Kennicutt et al. (2009),

$$L_{H\alpha}^{corr} \, (\text{erg s}^{-1}) = L_{H\alpha} + 0.020 \, L_{24\,\mu m} \, (\text{erg s}^{-1}). \quad (1)$$

For the Brown et al. (2014) subsample this was straightforward considering that the SEDs for their galaxies were given in the rest frame. For the O'Dowd et al. (2009) and Shipley et al. (2013) subsamples we used the best-fit SEDs (see Section 3.5) in the rest frame for each galaxy and again estimated the rest 24 μm flux densities from the SEDs for each galaxy. This was necessary for these two samples to be consistent with each other as a significant amount of the galaxies' IRS spectra at rest-frame 24 μm are shifted out of the observed IRS spectrum or dominated by noise owing to the redshift of the galaxies (49/142 galaxies for the combined samples). For the O'Dowd et al. (2009) and Shipley et al. (2013) samples, we synthesized MIPS 24 μm broadband flux densities by computing the (rest-frame) MIPS bandpass-weighted average flux density from the IR SED that best fit the long-wavelength photometry.[12]

In most cases the Hα extinction corrections are substantial. Figure 3 shows the relation between the corrected Hα luminosity and the ratio of observed Hα luminosity (uncorrected for dust extinction) to the extinction-corrected Hα luminosity. Most of the galaxies in our primary and a few in the secondary calibration samples have corrections of more than a factor of 2 to the Hα luminosity. The median correction factor is 4.2 and the interquartile range (25%−75%) is 2.5−5.9.

In Figure 4, we compare our extinction corrections from the monochromatic 24 μm luminosity with extinction-corrected Hα luminosities from the Balmer decrement, measured from

---

[11] See http://www.mpa-garching.mpg.de/SDSS/DR7/.

[12] See http://irsa.ipac.caltech.edu/data/SPITZER/docs/dataanalysistools/cookbook/14/.

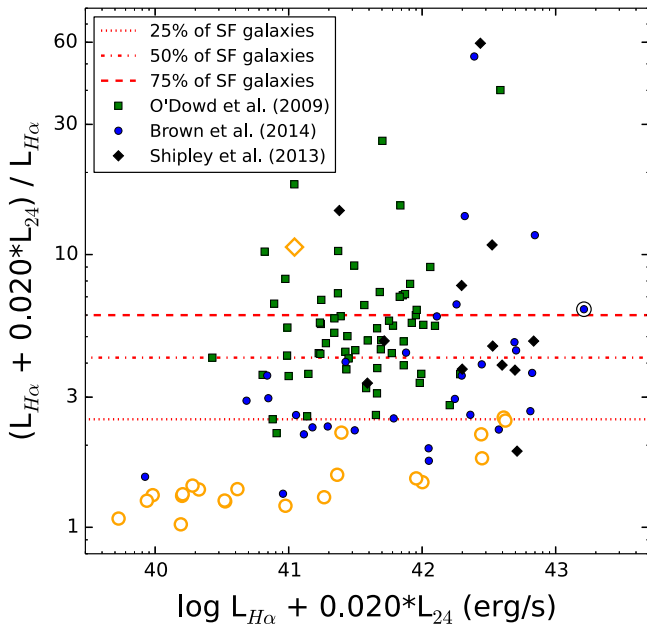**Figure 3.** Relation between the extinction-corrected Hα luminosity and the dust correction factor, defined as the ratio of the extinction-corrected Hα to observed (uncorrected) Hα. The filled symbols show the primary calibration sample. The horizontal lines show the 25%, 50%, and 75% of the distribution. The median correction factor is 4.2, and the interquartile range (25%−75%) is 2.5–5.9. The open orange symbols show the secondary calibration sample of low-metallicity galaxies as defined in Section 3.4. The blue point enclosed by a black circle denotes II Zw 096; see Section 4.4.

Figure 4. Extinction-corrected Hα luminosities corrected from the Balmer decrement (ratio of Hα/Hβ) compared to the extinction-corrected Hα luminosities corrected from the 24 μm luminosity for the primary calibration sample. We denote galaxies with $A_{Hα} > 1$ mag (open circles). We performed unity (black dashed line) and linear (green dashed line) fits to the galaxies with $A_{Hα} \leqslant 1$ mag. For many sources the results are consistent. However, there is a sample of highly attenuated objects, $A_{Hα} > 1$ mag, where we see big deviations (see Section 3.3 for further explanation). Three galaxies from the primary calibration sample do not appear in the figure owing to unreliable Hβ flux measurements.

Figure 5. Histogram of the metallicities for all the star-forming galaxies in the calibration sample, where the metallicities are $12 + \log(\text{O/H})_{N2}$. For the calibration of the SFR relations using PAH luminosity we used galaxies with $12 + \log(\text{O/H})_{N2} \geqslant 8.5$ (red dashed line) for our primary calibration sample, the resulting cut being 0.65 of the solar abundance ($12 + \log(\text{O/H}) = 8.69$; Asplund et al. 2009; orange dashed line).

the ratio of the Hα and Hβ emission lines. Most of our primary calibration sample consists of dusty star-forming galaxies (i.e., LIRGs) that heavily attenuate the Hβ emission line and to a lesser extent the Hα emission line. We indicate galaxies with $A_{Hα} > 1$ mag, which, in essence, results in an attenuation factor of $\gtrsim 2.5$ for Hα and a factor $\gtrsim 3.6$ for Hβ. For many sources the results are consistent. However, there is a sample of highly attenuated objects, $A_{Hα} > 1$ mag, where we see big deviations (at the higher extinction-corrected Hα luminosities the Balmer decrement corrections saturate). The likely explanation for this attenuation is that the interstellar medium (ISM) at Hβ is optically thick, so we are only seeing the "skin" of the star-forming region (down to where $τ \sim 1$ for Hβ), whereas we can see deeper into the star-forming region for Hα. Balmer absorption could be another issue. Figure 4 suggests that it is a significant contributor, since there are many galaxies where correcting with the Balmer decrement overcorrects Hα. Only about half the sources in the primary calibration sample for $A_{Hα} > 1$ mag allow us to extinction correct using the Balmer decrement, and ~10% of the sample have unreliable corrections owing to Hβ being heavily attenuated. For this reason, we adopt the $L_{Hα} + 0.020 \times L_{24\,μm}$ method as the best estimator for the total Hα emission for our primary calibration sample.

3.4. Gas-phase Metallicities

The PAH emission from a galaxy is known to depend on the gas-phase metallicity. Engelbracht et al. (2005) demonstrated this dependence using 8–24 μm ratios of galaxies above and below a metallicity of $12 + \log(\text{O/H}) = 8.2$, where they attributed the smaller ratios for galaxies with low metallicity to a decrease in the mid-IR emission bands (attributed to PAHs).
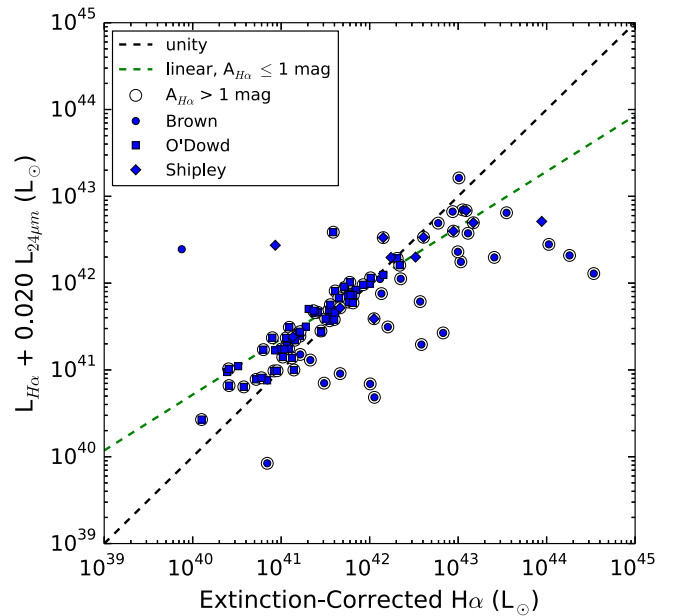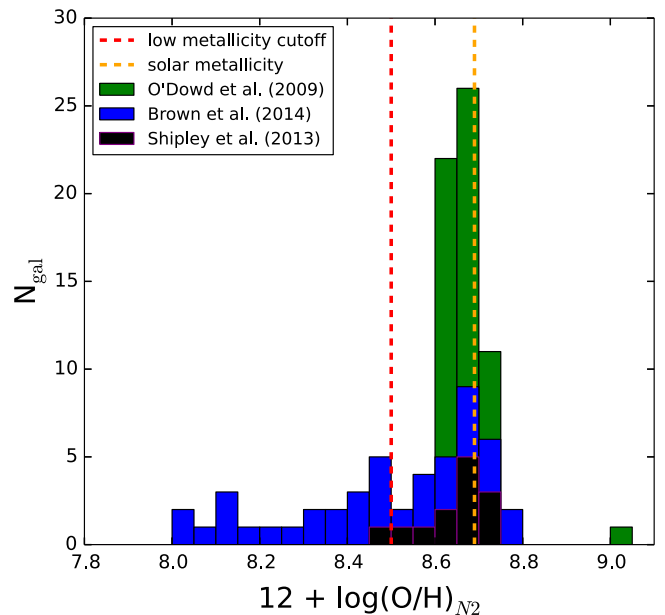
Calzetti et al. (2007) showed that star-forming galaxies with low metallicities have less-than-expected mid-IR dust emission (presumably from PAH emission) based on a linear fit to their calibration of extinction-corrected Paα to the 8 μm dust

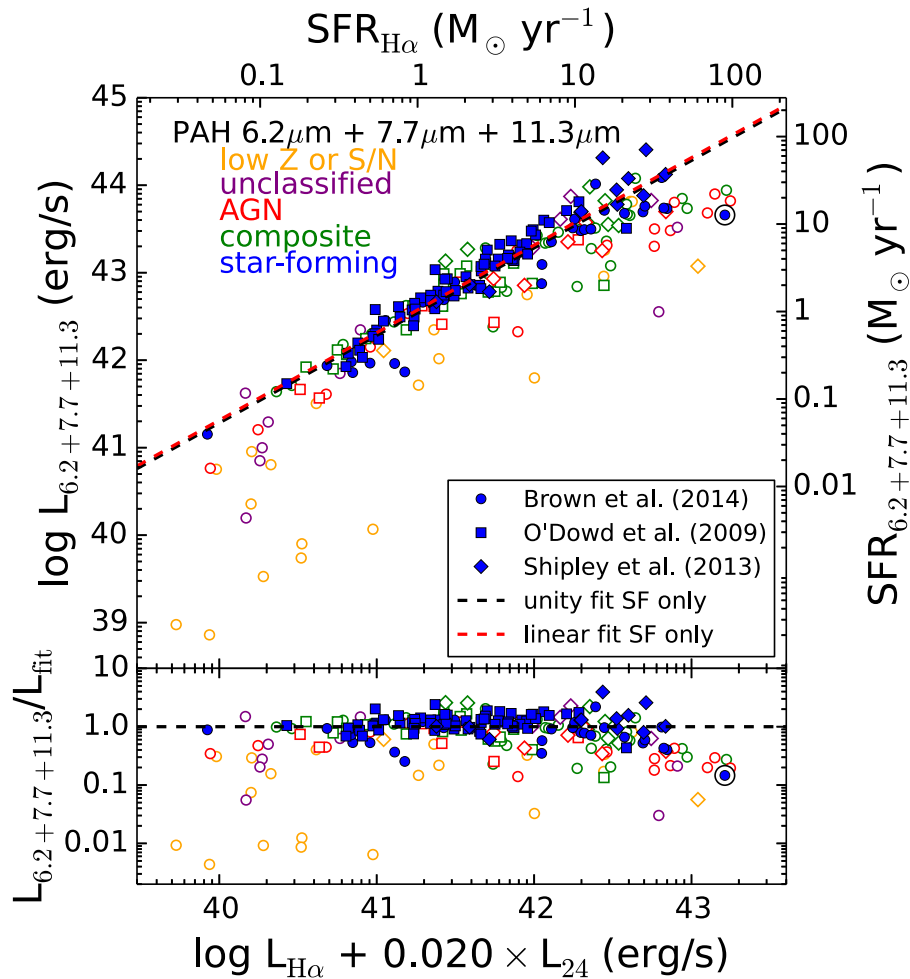**Figure 6.** Top: extinction-corrected Hα luminosity ($L_{Hα} + 0.020 \times L_{24\,μm}$) vs. total PAH luminosity ($L_{6.2\,μm} + L_{7.7\,μm} + L_{11.3\,μm}$ PAH features). We fit a unity relation (dashed black line) to the primary calibration sample (filled blue points) and use this line (that we define as L_{fit}) to show the ratio of the total PAH luminosity, for each galaxy, to the unity relationship as a function of extinction-corrected Hα luminosity (bottom panel). We classify galaxies as star-forming (filled blue points), composite (unfilled green points), or an AGN (unfilled red points) based on the location of their emission-line ratios on a BPT diagram. Unclassified galaxies (unfilled purple points) did not have all lines required for BPT classification, and the star-forming galaxies with low metallicity or S/N (unfilled orange points) are not used for the PAH SFR calibration (filled blue points; see the text for more details). The blue point enclosed by a black circle denotes II Zw 096; see Section 4.4.

emission. This trend is not seen in their calibration of extinction-corrected Paα to Hα + 24 μm luminosities, illustrating the PAH emission dependence on metallicity.

We calibrate the relation between metallicity, PAH emission, and SFRs using the data in our samples. For all galaxies in the calibration sample, we estimate the gas-phase oxygen abundance using the $N2$ index, $N2 \equiv \log [\text{N\,\textsc{ii}}]\,λ6583/Hα$, using the relation from Pettini & Pagel (2004),

$$12 + \log(\text{O/H}) = 8.90 + 0.57 \times N2. \tag{2}$$

We use $12 + \log(\text{O/H})_{N2}$ because the $N2$ index is available for all galaxies in our calibration sample. Figure 5 shows the distribution of oxygen abundance for the galaxies in our primary and secondary calibration samples. Most sources fall in a tight distribution (±0.2 dex) around the solar abundance (12 + log(O/H) = 8.69; Asplund et al. 2009) with a long tail to lower abundances. This is unsurprising because of the well-known mass–metallicity relation (Tremonti et al. 2004). Most sources in the calibration samples have $L_{IR} > 10^{10}\,L_{\odot}$ and likely have higher stellar mass and therefore higher abundance

(e.g., based on Tremonti et al. 2004, galaxies with stellar mass $>10^9\,M_{\odot}$ have abundances >0.5 $Z_{\odot}$). We use star-forming galaxies with $12 + \log(\text{O/H})_{N2} \geqslant 8.5$ for the primary calibration sample.

3.5. Total IR Luminosity

We estimate the total IR luminosity ($L_{IR} = L_{8-1000\,μm}$) using the MIPS 24 μm flux densities (also 70 and 160 μm, where available in Shipley et al. 2013) and the method in Shipley et al. (2013). We use the Rieke et al. (2009) IR SEDs because for star-forming galaxies the total IR luminosities derived from these templates using the 24 μm flux density only are closest to the IR luminosities derived when more IR photometric bands are available. These results help us understand the range of total IR luminosity over which our PAH SFRs are calibrated; our calibration may not extend to higher IR luminosities, where the PAH features tend to be suppressed. We were able to determine the contributing total IR luminosity range for the Brown et al. (2014) sample by using the values reported in Haan et al. (2013) for the majority of the galaxies.

4. THE PAH SFR CALIBRATION

Previous studies have shown that the Hα luminosity is a robust indicator of the SFR once corrected for dust extinction, but this correction is nontrivial (e.g., Kennicutt 1998). More recent work has shown that the Hα luminosity summed with a fraction of the monochromatic 24 μm light provides a linear fit against extinction-corrected Hα and Paα emission (Calzetti et al. 2007; Kennicutt et al. 2007, 2009; Treyer et al. 2010). Here we use the extinction-corrected Hα from the 24 μm monochromatic emission as our SFR calibrator, using Kennicutt et al. (2009),

$$\text{SFR} (M_\odot \text{ yr}^{-1}) = 5.5 \times 10^{-42}[L(\text{H}\alpha) + 0.020\, L(24\,\mu\text{m})] \times (\text{erg s}^{-1}), \tag{3}$$

where the constant of proportionality is appropriate for the Kroupa IMF we have adopted.

4.1. PAH SFR Relations

We compare the relation between the luminosity in the PAH features with the extinction-corrected Hα luminosity. Because different PAH features are accessible at different wavelengths depending on the redshift of the source and wavelength capabilities of the telescope/instrument, we calibrate the individual features at 6.2, 7.7, and 11.3 μm, as well as sums of these features. It is also worth noting that Hα probes very young star formation from OB stars, whereas it is likely that the PAH features cover a broader range of ages (presumably including contributions from A and early F stars) and that different SFR indicators are sensitive to slightly different effects from the star formation age range measured.

Figure 6 shows the correlation between the total PAH luminosity[13]

$$L_{\text{PAH}} = L_{6.2\,\mu\text{m}} + L_{7.7\,\mu\text{m}} + L_{11.3\,\mu\text{m}} \tag{4}$$

and the extinction-corrected Hα luminosity for the 227 galaxies in our calibration sample. For star-forming galaxies with high metallicity (primary calibration sample), the total PAH luminosity correlates linearly with the extinction-corrected Hα luminosity. Our derived relations between the extinction-corrected Hα luminosity and the total PAH luminosity are

$$\log L_{\text{PAH}} = (1.30 \pm 0.03) + \log(L_{\text{H}\alpha} + 0.020 \times L_{24\,\mu\text{m}}) \tag{5}$$

for the unity relation and

$$\log L_{\text{PAH}} = (1.30 \pm 0.03) + (1.00 \pm 0.03) \times \log(L_{\text{H}\alpha} + 0.020 \times L_{24\,\mu\text{m}}) \tag{6}$$

for the linear relation. We note that the forms of Equations (5) and (6) are essentially identical, and this is because the linear fit yields a slope consistent with unity to five significant digits (1.0003 $\pm$ 0.03). Using Equation (3), this yields the following

calibrations for the total PAH luminosity as an SFR indicator:

$$\log \text{SFR} (M_\odot \text{ yr}^{-1}) = (-42.56 \pm 0.03) + \log L_{\text{PAH}}(\text{erg s}^{-1}), \tag{7}$$

and using the linear fit we find

$$\log \text{SFR} (M_\odot \text{ yr}^{-1}) = (-42.56 \pm 0.03) + (1.00 \pm 0.03) \times \log L_{\text{PAH}}(\text{erg s}^{-1}), \tag{8}$$

showing that there is statistical uncertainty of $\approx$0.03 dex and scatter of $\approx$0.135 dex on the total PAH luminosity unity SFR relationship (where we remind the reader that this applies for galaxies of roughly solar metallicity and luminosities of $10^9 < L_{\text{IR}}/L_\odot < 10^{12}$).

We observe small offsets from the extinction-corrected $L_{\text{H}\alpha}$ and L_{PAH} calibration between the different calibration sub-samples. We measure average offsets of $L_{\text{PAH}}/L_{\text{fit}} = 0.06$, 0.06, and -0.10 for the O'Dowd et al. (2009), Shipley et al. (2013), and Brown et al. (2014) subsamples, respectively. This may imply that there is an additional systematic uncertainty of 0.1 dex (i.e., 20%) on the PAH SFR calibration from differences in aperture corrections or data processing and analysis.

The scatter about this relation for the primary calibration sample is very small, 0.14 dex, at least over the luminosity range of our sample. This implies that the total PAH emission correlates linearly with the SFR. The scatter is similar to that measured for other star formation indicators measured against each other (Kennicutt et al. 2009), indicating that the total PAH emission is of similar accuracy in determining SFRs.

Figure 6 shows that it was necessary to remove the low-metallicity (and low-S/N; S/N < 5) galaxies from our primary calibration sample. The low-metallicity (and low-S/N) galaxies have low $L_{\text{PAH}}/L_{\text{fit}}$ ratios (Figure 6, bottom), where L_{fit} is defined as the unity relation fit to the primary calibration sample for the expected luminosity of the PAH luminosity for a given $L_{\text{H}\alpha} + 0.020 \times L_{24\,\mu\text{m}}$ luminosity. We mark the galaxy II Zw 096 as it is an outlier in the figures (Figures 6, 7, and 9) but do not omit it as it does not significantly affect our calibration of the PAH features (we discuss this interesting galaxy in Section 4.4).

We also calibrate the luminosity from the individual PAH features and combinations of them as SFR indicators as in some cases only one or two PAH features may be useable to get an SFR, such as for high-redshift galaxies (see Section 6.2). Figure 7 shows the relations between the extinction-corrected Hα luminosity and the individual PAH features and the total PAH luminosity for the primary calibration sample. Figure 8 shows the distribution of residuals between the PAH luminosity and the fit and shows both the scatter computed from the median absolute deviation (MAD; Beers et al. 1990) and a Gaussian fit, both of which are consistent. The scatter is smallest, $\sigma_{\text{MAD}} = 0.14$ dex (i.e., 40%), whenever the 7.7 μm feature is involved in the fit. This implies that this feature may provide the most robust measure of the SFR. The relation against the 6.2 μm feature has the highest scatter, $\sigma_{\text{MAD}} = 0.21$ dex (i.e., 60%), which may indicate more variation in galaxies between the luminosity in this feature and the SFR.
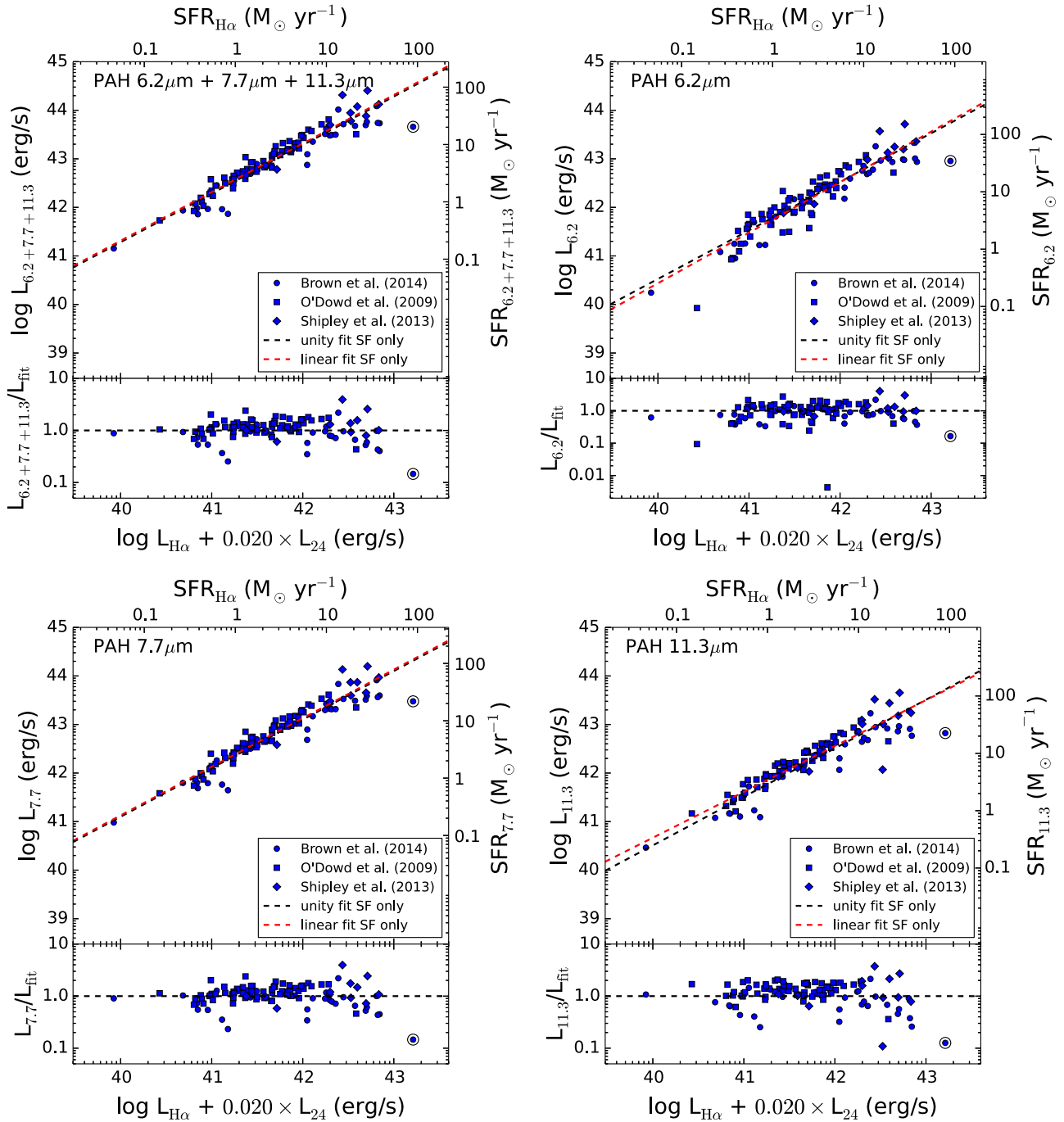
---

[13] L_{PAH} we use to denote the PAH luminosity for the total luminosity of the 6.2, 7.7, and 11.3 μm features. All other instances of PAH luminosity will be denoted by the included PAH features (e.g. $L_{6.2\,\mu\text{m}}$). However, in figures, we label explicitly which features are used.

Figure 7. Extinction-corrected Hα luminosity ($L_{H\alpha} + 0.020 \times L_{24\,\mu m}$; Kennicutt et al. 2009) vs. L_{PAH} (top left) and for the 6.2 μm (top right), 7.7 μm (bottom left), and 11.3 μm (bottom right) PAH features separately. This illustrates that the small scatter persists for the individual PAH features ($\sigma_{MAD} \lesssim 0.2$ dex). We fit a unity relation to the primary calibration sample (solid black line) and use this line as L_{fit} to determine residuals of expected L_{PAH} values (bottom for each panel). We used this fit to determine an SFR relation for L_{PAH} and each PAH feature shown individually (see Section 4.1). The blue point enclosed by a black circle denotes II Zw 096; see Section 4.4.

Our derived relations between the extinction-corrected Hα luminosity and the individual PAH luminosities are

$$\log L_{6.2\,\mu m} = (0.47 \pm 0.08)$$
$$+ \log(L_{H\alpha} + 0.020 \times L_{24\,\mu m})$$
$$\log L_{7.7\,\mu m} = (1.11 \pm 0.05)$$
$$+ \log(L_{H\alpha} + 0.020 \times L_{24\,\mu m})$$
$$\log L_{11.3\,\mu m} = (0.54 \pm 0.07)$$
$$+ \log(L_{H\alpha} + 0.020 \times L_{24\,\mu m}) \quad (9)$$

for the unity relations, and the linear relations are

$$\log L_{6.2\,\mu m} = (-1.20 \pm 0.09) + (1.04 \pm 0.04)$$
$$\times \log(L_{H\alpha} + 0.020 \times L_{24\,\mu m})$$
$$\log L_{7.7\,\mu m} = (1.12 \pm 0.06) + (1.00 \pm 0.03)$$
$$\times \log(L_{H\alpha} + 0.020 \times L_{24\,\mu m})$$
$$\log L_{11.3\,\mu m} = (2.87 \pm 0.08) + (0.94 \pm 0.03)$$
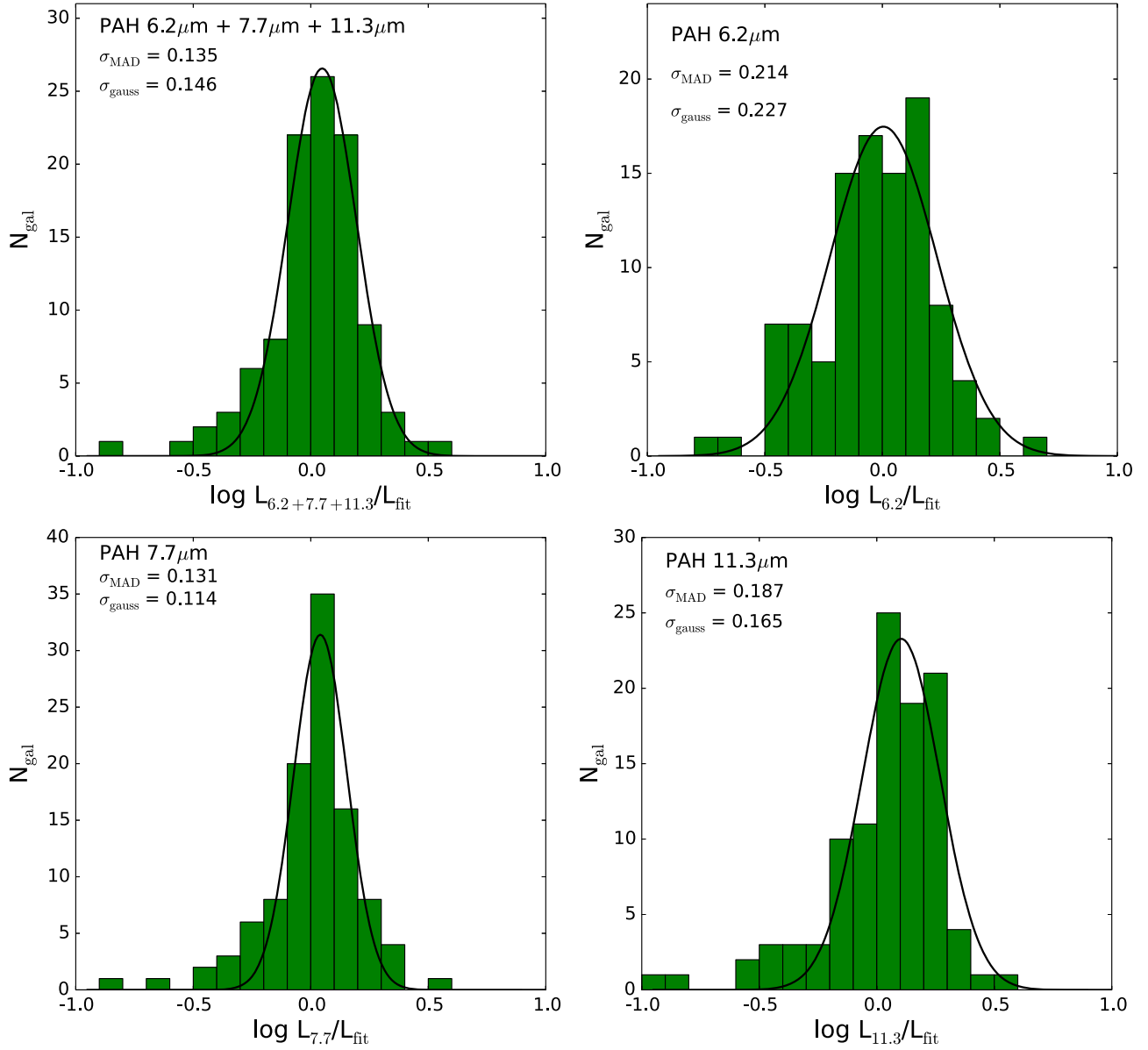$$\times \log(L_{H\alpha} + 0.020 \times L_{24\,\mu m}). \quad (10)$$

Figure 8. Histogram of the ratio of L_{PAH}/L_{fit}, where L_{fit} is the unity relation to the star-forming galaxies shown in Figure 7, demonstrating the scatter in the sample and consistency of L_{PAH} as an SFR indicator in comparison to extinction-corrected Hα for the 6.2 μm (top right), 7.7 μm (bottom left), and 11.3 μm (bottom right) PAH features individually and L_{PAH} (top left). The bin size used is 0.1 log L_{PAH}/L_{fit}, and N_{gal} represents the number of galaxies in each bin. We fit a Gaussian distribution to determine the standard deviation of the scatter (σ_{gauss}, shown in plot) and calculated the median absolute deviation (σ_{MAD}) to represent accurately the scatter of $L_{PAH,\lambda}$ as an SFR indicator.

In every instance, the linear relations are consistent with a unity slope between the PAH luminosities and the SFR (within 2σ of unity). Again, using the relation from Kennicutt et al. (2009) given in Equation (3), this yields the following calibrations for the individual PAH luminosities as SFR indicators:

$$\log \text{SFR } (M_\odot \text{ yr}^{-1}) = (-41.73 \pm 0.08)$$
$$+ \log L_{6.2\,\mu\text{m}} (\text{erg s}^{-1})$$

$$\log \text{SFR } (M_\odot \text{ yr}^{-1}) = (-42.37 \pm 0.05)$$
$$+ \log L_{7.7\,\mu\text{m}} (\text{erg s}^{-1})$$

$$\log \text{SFR } (M_\odot \text{ yr}^{-1}) = (-41.80 \pm 0.07)$$
$$+ \log L_{11.3\,\mu\text{m}} (\text{erg s}^{-1}), \qquad (11)$$

and using the linear fits we find

$$\log \text{SFR } (M_\odot \text{ yr}^{-1}) = (-40.06 \pm 0.09) + (0.96 \pm 0.04)$$
$$\times \log L_{6.2\,\mu\text{m}} (\text{erg s}^{-1})$$

$$\log \text{SFR } (M_\odot \text{ yr}^{-1}) = (-42.38 \pm 0.06) + (1.00 \pm 0.03)$$
$$\times \log L_{7.7\,\mu\text{m}} (\text{erg s}^{-1})$$

$$\log \text{SFR } (M_\odot \text{ yr}^{-1}) = (-44.14 \pm 0.08) + (1.06 \pm 0.03)$$
$$\times \log L_{11.3\,\mu\text{m}} (\text{erg s}^{-1}).$$
$$(12)$$

All of these SFR relations, coefficients, and the scatter for each can be found in Tables 2 (unity relation defined as log SFR $[M_\odot \text{ yr}^{-1}] = C + \log L_{PAH,\lambda} \text{ [erg s}^{-1}]$) and 3

Table 2
Unity PAH Luminosity SFR Relations

PAH Feature(s)	C	σ_{MAD}
6.2 + 7.7 + 11.3	−42.56 ± 0.03	0.135
6.2	−41.73 ± 0.08	0.214
7.7	−42.37 ± 0.05	0.131
11.3	−41.80 ± 0.07	0.187
6.2 + 7.7	−42.47 ± 0.04	0.135
6.2 + 11.3	−42.09 ± 0.04	0.160
7.7 + 11.3	−42.48 ± 0.04	0.120

Note. The calibration sample consisted of 105 galaxies used to determine the PAH SFR relations (see Section 2.1). Column (1) defines which PAH features were used in the SFR relation. Column (2) gives the values for the unity SFR relations (defined as log SFR $[M_\odot \, yr^{-1}] = C + \log L_{PAH,\lambda}$ [erg s^{-1}]). Column (3) is the 1σ scatter in the SFR relation for the galaxies used in the fit (using the median absolute deviation, MAD [σ_{MAD}], to represent the scatter).

Table 3
Linear PAH Luminosity SFR Relations

PAH Feature(s)	A	B	σ_{AB}	σ_{MAD}
6.2 + 7.7 + 11.3	−42.56 ± 0.03	1.00 ± 0.03	−0.03	0.138
6.2	−40.06 ± 0.09	0.96 ± 0.04	−0.07	0.233
7.7	−42.38 ± 0.06	1.00 ± 0.03	−0.03	0.138
11.3	−44.14 ± 0.08	1.06 ± 0.03	−0.04	0.166
6.2 + 7.7	−42.05 ± 0.04	0.99 ± 0.03	−0.03	0.137
6.2 + 11.3	−42.52 ± 0.05	1.01 ± 0.03	−0.04	0.144
7.7 + 11.3	−42.85 ± 0.04	1.01 ± 0.03	−0.03	0.139

Note. The calibration sample consisted of 105 galaxies used to determine the PAH SFR relations (see Section 2.1). Column (1) defines which PAH features were used in the SFR relation. Columns (2) and (3) give the values for the linear SFR relations (defined as log SFR $[M_\odot \, yr^{-1}] = A + B \log L_{PAH,\lambda}$ [erg s^{-1}]). Column (4) is the 1σ measurement in the covariance of the linear fit (see Section 4.2). Column (5) is the 1σ scatter in the SFR relation for the galaxies used in the fit (using the median absolute deviation, MAD [σ_{MAD}], to represent the scatter).

(linear relation defined as log SFR $[M_\odot \, yr^{-1}] = A + B \log$ $L_{PAH,\lambda}$ [erg s^{-1}]), which includes all possible PAH feature combinations. We note there are two galaxies (galaxies SSGSS 52 and 83 from the sample of O'Dowd et al. 2009) for the 6.2 μm calibration that are well off the relation. We attribute this to the "problematic 6.2 μm feature fits" discussed in O'Dowd et al. (2009). These galaxies did not affect our calibration of the 6.2 μm feature, and the uncertainties decrease only slightly when excluding them from the PAH SFR relations.

4.2. Uncertainties for Derived SFR Relations

We determined uncertainties for our PAH SFR relations using a robust linear fit to the 105 galaxies in the primary calibration sample that utilizes a least-squares fitting routine. This routine determines residuals for the fit of the luminosities and estimates a 1σ uncertainty on the mean of the estimated values returned for the fit (slope and intercept for the linear fits). We then propagate these uncertainties for the derived PAH SFR relations. The slope and intercept are covariant, and we report the covariance matrix for these fits in Table 3, where
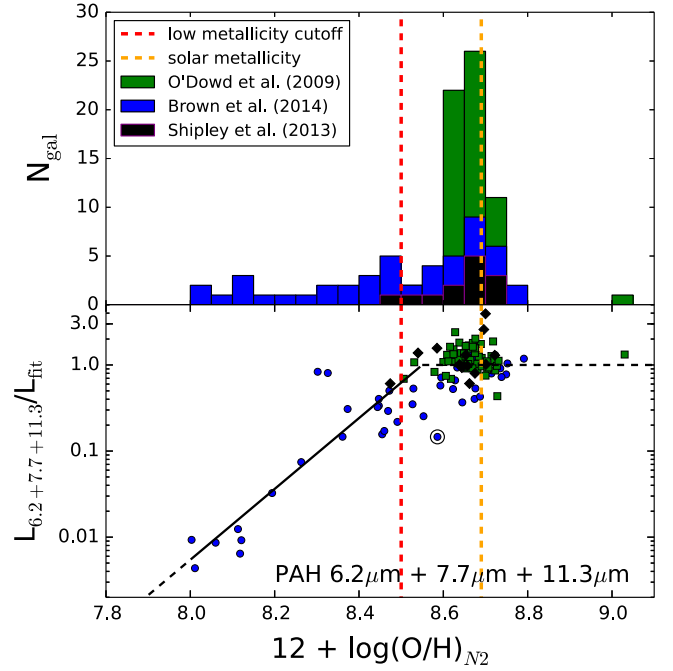

Figure 9. Top: same metallicity distribution for the star-forming galaxies in the calibration sample as Figure 5. Bottom: L_{PAH}/L_{fit} ratios for the star-forming galaxies as a function of oxygen abundance. This shows how the low-metallicity galaxies result in weaker observed PAH emission than expected from the correlation. For the corrections to the PAH luminosity we used galaxies with $12 + \log(O/H)_{N2} \leqslant 8.55$. We determined a correction to the PAH luminosity by fitting a line (solid black line) for the galaxies below Z_0 ($Z_0 = Z_\odot - 8.55 = -0.14$) and extrapolations (dashed black lines) beyond the sample limit (low end) and the fit (high end; see Section 4.3 for more details). The blue point enclosed by a black circle denotes II Zw 096; see Section 4.4.

the covariance matrix has the following form:

$$\text{cov} = \begin{pmatrix} \sigma_A^2 & \sigma_{AB} \\ \sigma_{AB} & \sigma_B^2 \end{pmatrix}. \quad (13)$$

The fact that the off-diagonal elements of the covariance matrix are negative means that A and B are not independent and are anticorrelated. The diagonal elements are the variance on parameters A and B.

4.3. Correction to PAH Luminosity for Low-metallicity Galaxies

For our secondary calibration sample of 25 galaxies, we limited the oxygen abundance of the galaxies to $12 + \log(O/H)_{N2} \leqslant 8.55$, as shown in Figure 9. This figure shows that galaxies at lower oxygen abundances have lower PAH luminosities compared to that expected from our fit between the total PAH luminosity and extinction-corrected Hα for the higher-metallicity galaxies. While the metallicity cut between the primary and secondary calibration samples is arbitrary, it defines the location where we start to observe a break in the L_{PAH}/L_{fit} ratios in Figure 9. The strength of the PAH features is known to decline with decreasing metallicity (Engelbracht et al. 2005; Calzetti et al. 2007), which is likely driving the trend.

We fit the secondary calibration sample with a robust linear fit routine (same as the PAH SFR relations) as shown in Figure 9 for $12 + \log(O/H)_{N2} \leqslant 8.55$. We derive metallicity-

Table 4
Metallicity Corrections

PAH Feature(s)	A
6.2 + 7.7 + 11.3	4.1 ± 0.3
6.2	4.0 ± 0.3
7.7	4.0 ± 0.3
11.3	3.7 ± 0.3
6.2 + 7.7	4.1 ± 0.4
6.2 + 11.3	3.8 ± 0.3
7.7 + 11.3	4.1 ± 0.3

Note. Column (1) defines which PAH features were used for the fit (see Figure 9, bottom). Column (2) gives the linear relation coefficients for the metallicity corrections (defined as $\log L_{PAH,\lambda}^{corr} = \log L_{PAH,\lambda} - A[Z - (Z_\odot + Z_0)]$, where $Z_0 = -0.14$). Note that metallicity corrections are for galaxies with $Z \leqslant Z_\odot + Z_0$.

dependent corrections to the PAH luminosity for each PAH combination as

$$\log L_{PAH,\lambda}^{corr} = \log L_{PAH,\lambda} - A[Z - (Z_\odot + Z_0)] \qquad (14)$$

for $12 + \log(O/H)_{N2} \leqslant 8.55$. We define $Z_0 = Z_\odot - 8.55 = -0.14$. We do not have a sufficient number of low-metallicity star-forming galaxies to determine whether the fit between metallicity and $L_{PAH,\lambda}/L_{fit}$ is linear or more complex. For galaxies with $12 + \log(O/H)_{N2} > 8.55$, we force the ratio of L_{PAH}/L_{fit} to be unity. We need more supersolar-metallicity galaxies to determine whether this assumption is accurate. The metallicity corrections for each combination of PAH features are listed in Table 4.

4.4. The Interesting Galaxy: II Zw 096

II Zw 096 is a high-luminosity galaxy ($L_{IR} \sim 10^{12} L_\odot$; Goldader et al. 1997; Inami et al. 2010; Haan et al. 2013) with $12 + \log(O/H)_{N2} = 8.59$, which implies a metallicity of $0.8 Z_\odot$. It is currently in the process of a merger (Inami et al. 2010; Brown et al. 2014). The PAH luminosity is much lower than that expected from our SFR calibration, and this makes II Zw 096 an interesting case study. Our primary calibration sample includes other merging systems (NGC 6090 and possibly SSGSS 18; Brown et al. 2014; Battisti et al. 2015) that lie on the relations, and thus the behavior of II Zw 096 is unique within our sample.

Inami et al. (2010) showed that the huge luminosity of this galaxy does not originate in its nucleus, but is from Region D (67% of the 24 μm flux), well removed from the visible traces of the interacting galaxies. The diameter of this source is only a few hundred parsecs, and its luminosity is $\sim 7 \times 10^{11} L_\odot$, so conditions within it are likely to resemble those in the nuclei of local ULIRGs, where it is well established that the PAH features are suppressed (e.g., Rieke et al. 2009). Additional discussion of the unique characteristics of this object can be found in Inami et al. (2010); see also Section 5 below. However, we conclude that the deviation from the PAH SFR calibration is not surprising, given these characteristics. It nonetheless serves as a warning of rare conditions that can affect the accuracy of the derived SFRs.

4.5. Photometric Calibrations of the 7.7 μm PAH Feature Using Broadband Photometry

Many galaxies observed with *Spitzer* imaging do not have spectra, and *JWST* faint imaging will also focus on objects too distant and faint for efficient spectroscopy. We have therefore performed photometric calibrations assuming rest-frame *Spitzer*/IRAC 8 μm and *JWST*/MIRI 7.7 μm filters, to determine the accuracy of (rest-frame) mid-IR photometry that covers the PAH features as a possible SFR tracer. The comparison of the two photometric bands provides a cross-calibration and also lets us assess systematic effects in the photometry. We estimated broadband flux densities for the filters from the rest-frame spectra of the primary calibration sample of star-forming galaxies. To measure the rest-frame IRAC and MIRI flux densities, we followed the same procedure as for the 24 μm broadband, rest-frame flux densities (see Section 3.3). Then we followed the same procedure for the SFR calibrations of the PAH features (Section 4) to derive the photometric SFR relations. Figure 10 shows the relation between the synthesized (rest-frame) IRAC 8 μm and MIRI 7.7 μm bands and the extinction-corrected Hα luminosity. The relations are consistent with linear, where the derived relations between the extinction-corrected Hα luminosity and the *Spitzer*/IRAC 8 μm band are

$$\log SFR (M_\odot \ yr^{-1}) = (-42.99 \pm 0.06) + \log L_{8\,\mu m} (erg \ s^{-1}) \qquad (15)$$

for the unity relation ($\sigma_{MAD} = 0.166$) and

$$\log SFR (M_\odot \ yr^{-1}) = (-42.79 \pm 0.07) + (0.995 \pm 0.030) \log L_{8\,\mu m} (erg \ s^{-1}) \qquad (16)$$

for the linear relation ($\sigma_{MAD} = 0.132$). The derived relations between the extinction-corrected Hα luminosity and the *JWST*/MIRI 7.7 μm band are

$$\log SFR (M_\odot \ yr^{-1}) = (-43.05 \pm 0.06) + \log L_{7.7\,\mu m} (erg \ s^{-1}) \qquad (17)$$

for the unity relation ($\sigma_{MAD} = 0.156$) and

$$\log SFR (M_\odot \ yr^{-1}) = (-42.84 \pm 0.07) + (0.995 \pm 0.031) \times \log L_{7.7\,\mu m} (erg \ s^{-1}) \qquad (18)$$

for the linear relation ($\sigma_{MAD} = 0.136$). The relations for both photometric bands compare very well to the 7.7 μm PAH feature calibration with slopes of nearly 1 and illustrate the ability for mid-IR photometry in bands dominated by PAHs to give accurate SFRs for samples of star-forming galaxies.

Yuan et al. (2011) show a tight relation between SFR and Akari 9 μm photometry, where they determined the SFRs by fitting templates that simultaneously accounted for the optical–UV and reradiated IR. Their relation is very similar to ours in Equation (16), i.e., converted to our units,

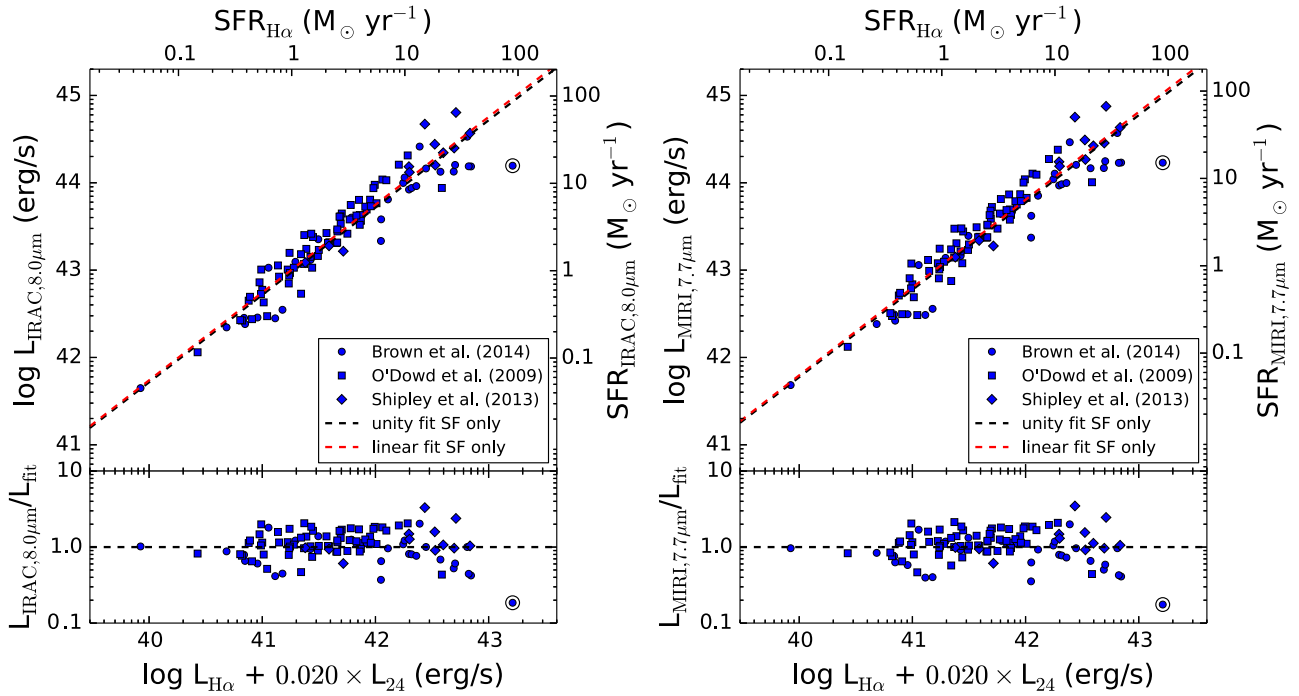$$\log SFR (M_\odot \ yr^{-1}) = (-42.61) + (0.99 \pm 0.03) \times \log L_{9\,\mu m} (erg \ s^{-1}) \qquad (19)$$

Figure 10. Same as Figure 7 but for the broadband photometric calibrations of the 7.7 μm PAH feature. The left panel is the calibration for the (rest-frame) *Spitzer*/IRAC 8 μm filter. The right panel is the calibration for the (rest-frame) *JWST*/MIRI 7.7 μm filter. The derived SFR relations from the two photometric calibrations are given in Section 4.5.
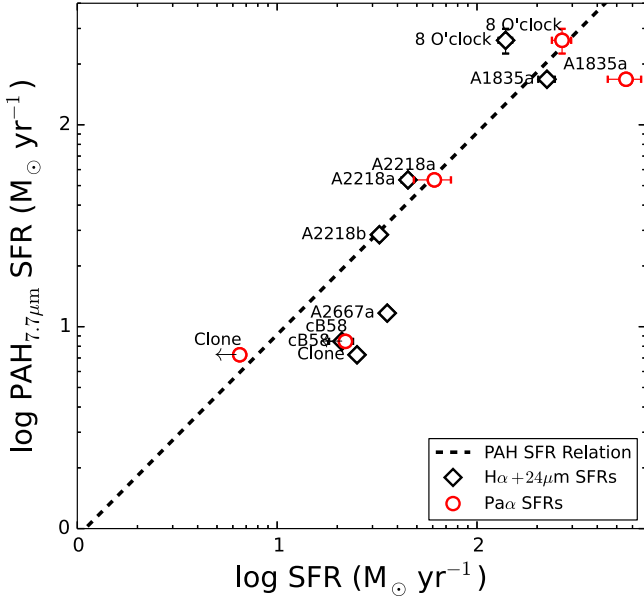

Figure 11. Estimated SFRs from the PAH 7.7 μm in comparison to the estimated Paα (open red circles) and Hα+24 μm (open black diamonds) SFRs for the demonstration sample (some of the statistical uncertainties are smaller than the symbol size, primarily for the vertical axis; see Section 6.2 for discussion). The line shown is the unity PAH 7.7 μm SFR relation from our primary calibration sample (Section 4.1) to the Paα and Hα+24 μm SFR relations.

but with a ∼0.2 dex offset. They show that this offset is a systematic effect (their Figure 11), probably due to differences in the photometric bands, so the agreement is virtually perfect.

These SFR estimates will not be accurate where an AGN dominates the galaxy emission near 7.7 μm. Three approaches can be used to eliminate this potential source of error. First, mid-IR spectroscopy will identify AGN-dominated galaxies

through the reduced equivalent widths of the PAH features. Second, such galaxies can be identified with ancillary data, such as deep X-ray imaging. Third, with multiband mid-IR photometry it should be possible to identify AGN-dominated cases as demonstrated by Teplitz et al. (2011) using *Spitzer* observations. The latter approach is based on identification of AGNs from the shape of their mid-IR SEDs (e.g., Lacy et al. 2004, 2007; Stern et al. 2005). For example, Donley et al. (2012) showed that AGNs can be identified reliably as IRAC "power-law" sources where AGNs have mid-IR spectral behavior of $f_\nu > \lambda^{-2}$. We discuss application of this to high-redshift galaxies in a later section (Section 6.4).

5. PREVIOUS PAH SFR CALIBRATIONS AT LOW REDSHIFT

We compare with previous calibrations for PAH features against various SFR indicators. We confine this section to galaxies at $z < 0.5$. There are additional limitations. First, our calibration has been carried out for galaxies with SFRs up to ∼100 $M_\odot$ yr^{-1}. More luminous low-redshift galaxies show substantial deviations from proportionality between mid-IR and total IR luminosities (e.g., Marcillac et al. 2008; Rigby et al. 2008; Rieke et al. 2009), behavior that is not captured in our calibration. Second, if there are AGNs in the calibration studies of other samples, their presence can affect the results by supplementing the signatures of star formation or by destroying the PAH carriers. Third, measurement of the strengths of the PAH features depends critically on the treatment of the mid-IR continuum, which varies significantly from study to study (e.g., Hernán-Caballero et al. 2009; Treyer et al. 2010). All the studies under discussion start from the relation reported by Kennicutt (1998), where we correct to a Kroupa IMF (using the factor of 0.7 as in Kennicutt et al. 2009) and for the larger

luminosity obtained from the *Spitzer* data,

$$\text{SFR}_{\text{Kroupa}} \, (M_\odot \, \text{yr}^{-1}) = 2.54 \times 10^{-44} L_{\text{IR},8-1000 \, \mu\text{m}} (\text{erg s}^{-1}). \tag{20}$$

The previous calibrations of the PAH features as an SFR indicator discussed below illustrate these points. However, given the diverse range of samples and the various methods used to derive previous PAH SFRs, it is remarkable that the difference in the calibrations is relatively small (less than a factor of 2 for non-ULIRGs, and even the ULIRG samples agree within a factor of a few). This possibly indicates that the PAH luminosity as an SFR indicator is generally robust regardless of redshift, sample selection, or calibration method (except for very high luminosities). This behavior points to its accuracy over a broad range of conditions. Indeed, in Section 6.2 we show tentative evidence that the PAH-derived SFRs for galaxies with ULIRG luminosities at $1 < z < 3$ agree with those derived from other SFR tracers. We expect our sample to provide the most robust calibration of the PAH features, at least over its luminosity range, because we have carefully selected our primary calibration sample to be star-forming galaxies with about solar metallicity over a broad range of luminosities (10^9–$10^{12} \, L_\odot$) and morphologies (from dwarf galaxies to large disk galaxies).

5.1. Treyer et al. (2010)

Treyer et al. (2010) performed an analysis similar to Kennicutt et al. (2009) for various Hα-to-IR luminosity ratios, for galaxies at $z \sim 0.1$. They found consistent ratios to those of Kennicutt et al. (2009), especially for the 24 μm luminosity and scatter, and derived a new IR luminosity SFR relation (see Treyer et al. 2010, for a detailed description of the derivation).

An important test is whether our calibration is reproducible. Treyer et al. (2010) use the SSGSS sample (O'Dowd et al. 2009), one of the three samples in our full calibration sample. As in our analysis, they also used PAHFIT to measure PAH luminosities. The two studies should therefore be in close agreement, but this is somewhat convoluted to demonstrate. Treyer et al. (2010) give the ratio of the 7.7 and 11.3 μm feature strengths to the total IR luminosity, which they base on *Spitzer* photometry. They also define the integrated luminosity from 3 to 1100 μm, which they describe as being 0.04 dex larger on average than the commonly used definition integrating from 8 to 1000 μm. However, Kennicutt et al. (2009) find that basing the L_{IR} calculation on *Spitzer*/MIPS data results in 24% larger values because the 160 μm band captures cold emission that is not apparent in *IRAS* measurements (out to 100 μm).

We equate Equation (20) to those in Equation (11) to obtain the relation between the PAH feature and total IR luminosity and correct to the 3–1100 μm luminosity; the resulting relations are

$$\log L_{7.7 \, \mu\text{m}} = (-1.27 \pm 0.05) + \log L_{3-1100 \, \mu\text{m}} \tag{21}$$

$$\log L_{11.3 \, \mu\text{m}} = (-1.84 \pm 0.07) + \log L_{3-1100 \, \mu\text{m}}. \tag{22}$$

Treyer et al. (2010) obtained normalization values of -1.204 ± 0.087 and -1.851 ± 0.071, in excellent agreement with the relations we derive.

5.2. Sargsyan & Weedman (2009)

Sargsyan & Weedman (2009) investigated the PAH luminosity as an SFR indicator for a sample of galaxies at $z < 0.5$ by calibrating the flux at the peak of the 7.7 μm PAH feature against the total IR luminosity using the Kennicutt (1998) IR SFR relation. Their motivation for using the peak of the emission feature is that the SFR can still be estimated from the observed PAH emission even if the wavelength coverage is limited or the spectra have poor S/N, as might be the case for high-redshift sources. Using the flux at the peak of the PAH features, however, does introduce possible issues with the measurement of the continuum contributions (for example, contribution from an AGN). Sargsyan & Weedman (2009) limited their sample to objects with EW(6.2 μm) $>0.4 \, \mu$m to exclude likely AGNs, and they measured a linear relation between the 7.7 μm flux and SFR, with a constant of proportionality smaller by 0.2 dex (with an uncertainty of 0.2 dex) from the one we derive here.

5.3. Diamond-Stanic & Rieke (2012)

Diamond-Stanic & Rieke (2012) used SED templates (Rieke et al. 2009) to derive an SFR for local galaxies from the 11.3 μm PAH feature, which showed evidence of being the most resistant to the influence of an AGN. We can use our calibration to test their assumption that the 11.3 μm feature correctly represents the SFR. This allows us to have confidence that for galaxies with an AGN (at least up to moderate-luminosity AGNs), we can accurately derive SFRs from the integrated luminosity of the PAH features, especially for the 11.3 μm feature.

From Ho & Keto (2007), and taking a nominal ratio of [Ne II] to [Ne III] (Pereira-Santaella et al. 2010), we find the typical relation between [Ne II] and SFR is

$$\log L_{[\text{Ne II}]} = -2.88 + \log L_{8-1000 \, \mu\text{m}}. \tag{23}$$

We put Equation (22) on the same basis as Equation (23) by correcting it to the *IRAS* luminosity parameters:

$$\log L_{11.3 \, \mu\text{m}} = -1.70 + \log L(\text{IRAS})_{8-1000 \, \mu\text{m}}. \tag{24}$$

Comparing, we obtain an estimate that the ratio of fluxes is f ([Ne II]/f(11.3 μm) ~ 0.07, with errors of perhaps a factor of two. Farrah et al. (2007) find a value of 0.17 for a sample of local ULIRGs, again with an error of a factor of about two. Their value may be overestimated (by a factor of about two) because they subtracted the continuum with a spline fit rather than using an approach similar to that of PAHFIT (e.g., Hernán-Caballero et al. 2009; Treyer et al. 2010). These values are comparable to that of f([Ne II])/f(11.3 μm) = 0.12 found around moderate-luminosity AGNs by Diamond-Stanic & Rieke (2010). They determined the PAH feature strength through PAHFIT, so their result should be on the same scale as our calibration. This value should be dominated by emission associated with star formation, although a small contribution from the AGN may occur (Pereira-Santaella et al. 2010). In support of this conclusion, Alonso-Herrero et al. (2014) find that the 11.3 μm PAH feature seems to persist to within $\sim$200 pc of a number of AGNs. Thus, our calibration of SFRs from PAH features reinforces the conclusion that the 11.3 μm feature is not significantly reduced around moderate-luminosity

AGNs and can be used as a robust indicator of the SFR in these regions.

5.4. Pope et al. (2008)

Pope et al. (2008) derived linear relations between PAH features (6.2, 7.7, and 11.3 μm) and IR luminosity for a local sample of 22 galaxies with moderate-luminosity IR galaxies ($10^{10} < L_{\rm IR}/L_\odot \ 10^{12}$; Brandl et al. 2006) and high-redshift submillimeter galaxies (SMGs). Within the errors, the relations are consistent with ours (except that they indicate a lower value for the flux ratio $f[6.2 \ \mu{\rm m}]/f[7.7 \ \mu{\rm m}]$).

5.5. Farrah et al. (2007)

Farrah et al. (2007) derived a PAH SFR from a sample of 53 ULIRGs at $z < 0.3$, using the 6.2 and 11.3 μm PAH features, which they calibrate against the [Ne II] 12.81 μm and [Ne III] 15.55 μm emission lines. They focused on these features because they are relatively isolated spectrally and should be relatively easy to measure. They combined both features to mitigate variations in the strengths of individual PAH features between different starburst galaxies. The calibration of the PAH features with the [Ne II] + [Ne III] luminosity resulted in SFR ($M_\odot$ yr^{-1}) $= 1.18 \times 10^{-41} L_{\rm PAH}$ (erg s^{-1}), and then we converted it to the Kroupa IMF. The resulting conversion factor is an order of magnitude larger than our calibration. Part of this difference may arise from the use of spline fitting to remove the continuum, which has been shown to lead to underestimates of the PAH feature strengths by factors of 2–3 (e.g., Hernán-Caballero et al. 2009; Treyer et al. 2010), but much of it reflects that the PAH features in local ULIRGs tend to be suppressed.

6. APPLICATION TO DISTANT GALAXIES: A PREVIEW FOR *JWST*

IR SEDs evolve with redshift, so comparisons must be over similar redshift ranges or must make the necessary adjustments (e.g., Hernán-Caballero et al. 2009; Papovich et al. 2009; Elbaz et al. 2010; Finkelstein et al. 2011; Kirkpatrick et al. 2012; Rujopakarn et al. 2013). We first discuss previous works on this subject; in a following subsection we present results for our demonstration sample of gravitationally lensed, high-redshift galaxies as a case study for galaxies with luminosities and redshifts to be probed with *JWST*.

6.1. Previous Studies

6.1.1. Pope et al. (2008, 2013), Shi et al. (2009), Menéndez-Delmestre et al. (2009), and Fiolet et al. (2010)

From a sample of 13 SMGs, Pope et al. (2008) demonstrated that eight star-formation-dominated galaxies at $z \sim 2$ (seven ULIRGs) show linear correlations between $L_{\rm PAH}$ and $L_{\rm IR}$, very similar to those we have derived (the remaining SMGs showed evidence of AGNs). Additional calibrations of the PAH band strengths versus the IR luminosities of high-redshift galaxies have been reported by Shi et al. (2009), Menéndez-Delmestre et al. (2009), Fiolet et al. (2010), and Pope et al. (2013). Combining the 28 galaxies from the Pope et al. (2013) and Fiolet et al. (2010) samples, one can deduce that for $L_{\rm IR} \lesssim 3 \times 10^{12} L_\odot$ galaxies follow the relation between $L_{\rm PAH}$ and $L_{\rm IR}$ derived for our calibration sample. However, at greater IR luminosities, the high-redshift samples show lower $L_{\rm PAH}/L_{\rm IR}$ ratios. The difference in this regard with low-redshift

ULIRGs, which fall substantially below the proportional relationship by $10^{12} L_\odot$, is shown dramatically in Pope et al. (2013). The fact that the high-redshift galaxies fit on the low-redshift trend (albeit with significant scatter) up to such high luminosities supports other indications that at high redshifts the IR spectral properties even of highly luminous galaxies resemble those of moderate-luminosity low-redshift galaxies, rather than low-redshift galaxies of similarly high luminosity (e.g., Papovich et al. 2009; Hwang et al. 2010; Muzzin et al. 2010; Finkelstein et al. 2011). We discuss this behavior in more detail in the following section (Section 6.3).

6.1.2. Hernán-Caballero et al. (2009)

Hernán-Caballero et al. (2009) derived a PAH SFR relation using the $L_{\rm PAH}/L_{\rm IR}$ ratios of seven bright, starburst-dominated galaxies at $0.6 < z < 1.0$, using the Kennicutt (1998) IR SFR calibration. They derive SFR calibrations for each PAH feature (6.2, 7.7, and 11.3 μm). Compared to our results, their PAH SFR calibrations are larger by 0.15, 0.2, and 0.3 dex for the 6.2 μm, 7.7 μm, and 11.3 μm PAH features, respectively.[14] Their estimated PAH SFRs have uncertainties as large as factors of two (see Hernán-Caballero et al. 2009, for further discussion of issues that contribute to these uncertainties, as well as estimates from previous studies). It is difficult to evaluate their results further because they use an independent method to derive the PAH luminosities and measure the mid-IR continuum (and without a cross-calibration to PAHFIT it is not possible for a direct comparison to our results). They also derived total IR luminosities largely extrapolated from mid-IR flux densities, which may suffer systematics, further complicating any direct comparison. For the galaxies hosting quasars they find that the SFR estimated from the PAH features as a whole is 3–10 times less than indicated by the far-IR luminosities, suggesting either that the AGN contributes substantially to the far-IR and/or that the AGN destroys the PAH molecules.

6.1.3. Rujopakarn et al. (2013)

Rujopakarn et al. (2013) focus on the ability of 24 μm photometry to provide accurate estimates of SFRs out to $z \sim 3$. Thus, at the larger redshifts, they are probing the performance of the 7.7 μm PAH feature in this regard. Particularly for the stacked samples they find very good performance (e.g., their Figure 6) relative to their recommended far-IR SED. That is, the performance is not significantly redshift-dependent, indicating that there is a consistent SFR estimation regardless of the part of the spectrum being sampled from rest wavelengths of 6 to 24 μm. Wuyts et al. (2012) and Berta et al. (2013) have independently evaluated the prescription of Rujopakarn et al. (2013) against other star formation metrics and show very good agreement.

6.2. SFRs of High-redshift Lensed Galaxies

To probe the performance of the PAH bands as SFR indicators at lower luminosities, we now discuss the derived SFRs for the demonstration sample of lensed high-redshift galaxies (Section 2.2). For a comparison, we use the Hα

---

[14] The comparisons include a correction for the 11.3 μm PAH luminosity and the SFR, which is misreported in Hernán-Caballero et al. (2009) and should be SFR ($M_\odot$ yr^{-1}) $= 1.52 \times 10^{-8} L_{11.3 \ \mu{\rm m}}$ ($L_\odot$).

Table 5
Demonstration Sample SFRs

SFR Indicator	A2218b	A2667a	The Clone	A2218a	A1835a	cB58	8 O'clock
	$z = 1.034$	1.035	2.003	2.520	2.566	2.729	2.731
Paα	...	...	<6.5	61.2 ± 12.9	$557. \pm 105.$	<22.0	$266. \pm 29.4$
Hα + 24 μm	32.5 ± 1.3	35.5 ± 0.5	25.1 ± 1.5	45.1 ± 3.2	$223. \pm 21.2$	21.1 ± 2.9	$139. \pm 10.9$
6.2 + 7.7 + 11.3	27.2 ± 0.5	10.8 ± 0.3	8.3 ± 0.3	...	...	...	...
6.2	27.5 ± 0.3	8.1 ± 0.1	15.0 ± 0.6	68.6 ± 3.4	$211. \pm 39.4$	11.1 ± 0.8	$302. \pm 20.0$
7.7	28.5 ± 0.7	11.7 ± 0.4	7.3 ± 0.2	53.3 ± 1.3	$168. \pm 10.3$	8.5 ± 0.4	$262. \pm 36.7$
11.3	25.3 ± 1.0	11.4 ± 0.7	7.6 ± 1.2	...	...	...	...
6.2 + 7.7	27.9 ± 0.6	10.8 ± 0.3	8.6 ± 0.2	55.3 ± 1.2	$173. \pm 11.0$	8.8 ± 0.4	$265. \pm 29.6$
6.2 + 11.3	25.1 ± 0.5	9.4 ± 0.4	10.5 ± 0.7	...	...	...	...
7.7 + 11.3	27.7 ± 0.6	11.5 ± 0.4	7.3 ± 0.3	...	...	...	...

Note. Row 1 in the data gives the redshifts of the galaxies. Column (1) denotes the SFR indicator that was used to derive the SFR for each galaxy (PAH SFRs were estimated using the unity relations given in Table 2). Columns (2)−(8) are the estimated SFRs and uncertainties (at 1σ) of the flux measurements for each galaxy in the demonstration sample (see Section 6.2). All SFRs are in units of $M_\odot$ yr^{-1}.

+24 μm and Paα fluxes from Rujopakarn et al. (2012) to estimate SFRs. Although they report some measurements in Brα, the signal-to-noise ratio and the potential for systematic errors in line extraction due to the small equivalent widths of the latter line make it less useful. Kennicutt et al. (2009) demonstrate the effectiveness of Hα+24 μm as an extinction-free SFR indicator, while Paα is considered to be exceptionally accurate in this application because of the small extinction and the direct measure of the ionized gas. We have derived its strength relative to the shorter-wavelength H recombination lines assuming Case B recombination at electron temperature $T_e = 10,000$ K and density $N_e = 100\,\mathrm{cm}^{-3}$ (Osterbrock 1989), resulting in

$$\log \mathrm{SFR}\,(M_\odot\,\mathrm{yr}^{-1}) = (-40.33) + \log L_{\mathrm{Pa}\alpha}\,(\mathrm{erg\,s}^{-1}). \quad (25)$$

We compare these determinations with the PAH-derived values using the PAH SFR calibration in Table 2.

The results are summarized in Table 5 and Figure 11 gives a comparison of the various SFR indicators. We draw two main conclusions. First, the SFRs derived from the various PAH bands are generally consistent, indicating no significant change in their relative strengths with redshift. Second, the values derived from the PAH features are generally consistent with those from the other two indicators, typically within 0.3 dex (a factor of two). Moreover, in all cases the PAH luminosities have smaller uncertainties than the Paα measurements. This is because the PAH features are intrinsically brighter, and they will be among the brightest SFR indicators available for cosmologically distant galaxies.

For A1835a, the presence of an AGN seems likely given the emission-line ratio of $\log([\mathrm{N\,II}]/\mathrm{H}\alpha) \sim -0.25$ (Rujopakarn et al. 2012). An AGN would contribute to the Paα line flux without increasing the PAH fluxes, possibly contributing to the factor of about two higher SFR deduced from the line than from the PAH features. The degree of scatter is not terribly surprising given the scatter of each of the SFR indicators, plus potential issues such as hidden AGNs and systematic errors such as slit losses in the spectra measuring the H recombination lines, and the uncertain corrections for that problem.

6.3. The Validity of PAH-estimated SFRs for Very High Luminosity High-redshift Galaxies

Locally, there is evidence for a trend of decreasing PAH luminosity with increasing total IR luminosity that appears to
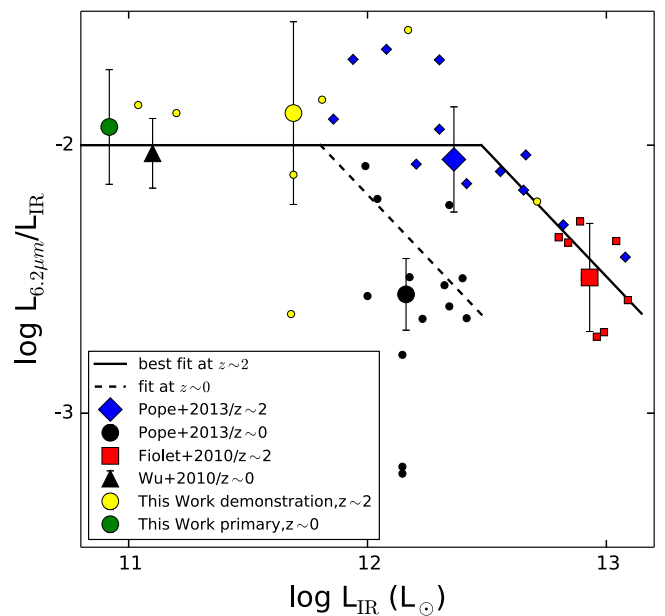

Figure 12. Comparison of low-redshift LIRG and ULIRG samples to high-redshift ($z \sim 2$) samples of LIRGs/ULIRGs. The low-redshift samples are from Pope et al. (2003, black circles), Wu et al. (2010, black triangle; median of sample), and the primary calibration sample (green circle, median of sample). The high-redshift samples are from Pope et al. (2013, blue diamonds), Fiolet et al. (2010, red squares) and the demonstration sample (yellow circles). We give a linear fit to the high-redshift ULIRGs (Fiolet et al. 2010; Pope et al. 2013), where a trend for decreasing $L_{6.2\,\mu m}/L_{\mathrm{IR}}$ becomes evident above $L_{\mathrm{IR}}/L_\odot \approx 3 \times 10^{12}$ (see Section 6.3 for fit parameters) and constant below this luminosity for $z > 1$. We use the same slope for the low-redshift ULIRGs for the trend seen at $z \sim 0$ for $L_{\mathrm{IR}}/L_\odot \approx 10^{12}$. Error bars are shown for the medians of the samples from the scatter in the samples (σ_{MAD}).

occur at an $L_{\mathrm{IR}} \gtrsim 10^{12}\,L_\odot$. This trend appears to be reduced for higher-redshift galaxies (e.g., Papovich et al. 2009; Muzzin et al. 2010; Finkelstein et al. 2011; Rujopakarn et al. 2011). The simplicity of applying observed frame 24 μm photometry to determining SFRs at high redshift depends on this trend being largely absent at high redshift, owing to the vigorous star formation being more extended and of lower surface density at high redshift (Rujopakarn et al. 2013). We now evaluate the luminosity range over which this behavior can be assumed.

To study this trend at higher redshift, we compared the PAH-to-total IR luminosities using our primary calibration sample and several samples of low-redshift LIRGs and ULIRGs (Wu

et al. 2010; Pope et al. 2013) with our demonstration sample of lensed galaxies and other samples of high-redshift LIRGs and ULIRGs ($z \sim 2$, Fiolet et al. 2010; Pope et al. 2013). Figure 12 gives the results of this relation as the total IR luminosity to the ratio of the luminosity of the 6.2 μm PAH feature over the total IR luminosity. We use the 6.2 μm feature as it is available for all samples considered here. All the samples use PAHFIT as we have done in this work, except for the Pope et al. (2013) sample, which has taken this into account by suggesting an increase of 1.7 to the PAH luminosities of their spline fitting method.

Figure 12 shows that the medians and scatters (σ_{MAD}) of the samples for the PAH-to-total IR luminosity ratios of high-redshift ULIRGs are more similar to low-redshift LIRGs rather than low-redshift ULIRGs, at least to $L_{IR} \approx 3 \times 10^{12} \, L_{\odot}$. This accounts for why the SFRs derived from the PAH features for the high-redshift lensed ULIRGs are consistent with the SFRs derived from Paα and Hα+24 μm. It also indicates that the low-redshift SFR calibration based on PAH luminosities is appropriate to use for high-redshift ULIRGs, even if it is not appropriate for low-redshift ULIRGs, consistent with other recent studies that have demonstrated this result (i.e., Rujopakarn et al. 2013). However, at even higher total IR luminosities ($L_{IR}/L_{\odot} \gtrsim 3 \times 10^{12}$), there is evidence that the L_{PAH}/L_{IR} ratio declines for the high-redshift samples (e.g., Fiolet et al. 2010). We fit this trend seen in Figure 12 as a broken power law and derive a linear fit above this luminosity using the high-redshift samples of Pope et al. (2013) and Fiolet et al. (2010), which yields

$$\log L_{6.2 \, \mu m}/L_{IR} = (9.7 \pm 0.4) + (-0.94 \pm 0.24)$$
$$\times \log L_{IR} \, (L_{\odot}) \quad \text{for } L_{IR} > 3 \times 10^{12} \, L_{\odot}.$$
(26)

The constant value below this luminosity is $\log L_{6.2 \, \mu m}/L_{IR} = -2.0 \pm 0.2$. We use the same slope for the low-redshift trend seen at an $L_{IR} \approx 10^{12} \, L_{\odot}$.

6.4. Use of JWST Photometry to Determine SFRs at High Redshift

We conclude that our PAH SFR calibration is accurate for high redshift ($1 < z < 3$) and for galaxies with SFRs up to $\lesssim 300 \, M_{\odot} \, yr^{-1}$ (corresponding to IR luminosities $\lesssim 3 \times 10^{12} \, L_{\odot}$). The calibration we derive in this paper for galaxies at $z < 0.4$ can be refined quickly with observations from JWST/MIRI, which will be sensitive to the PAH emission from distant galaxies out to $z \lesssim 2$. Therefore, our calibration will be very useful for studies with JWST of galaxies with dust-embedded star formation over a wide range of SFRs and over the peak of the SFR density in the universe (Madau & Dickinson 2014).

In cases where mid-IR spectroscopy is available, it will be possible to measure SFRs from PAH features directly. However, JWST mid-IR spectroscopy will be relatively inefficient as MIRI can observe only one object for each observation. Efficient SFRs for large numbers of galaxies should be possible from broadband imaging with MIRI provided that the samples can exclude AGNs (whose emission will contribute to the mid-IR emission). Three approaches can be used to eliminate this potential source of error as discussed earlier (Section 4.5). However, earlier work by Donley et al. (2008) showed that identification of power-law AGNs with

IRAC data becomes unreliable by $z \geqslant 1.75$ because the continua of stellar populations at the relevant rest wavelengths start to mimic power laws (see Donley et al. 2008, their Figure 5). This issue can be avoided by applying the power-law method at longer wavelengths. Multiwavelength observations with JWST can extend the power-law method so it can be applied at all relevant redshifts. One simple way to accomplish this would be to image at 3.56 μm (NIRCam) and with MIRI at 5.6, 10, 15, and 21 μm or a subset of these bands.[15] To get to equal depth in four shorter-wavelength bands as at 21 μm relative to a power law with an index of -2 takes very little extra time (only about 40% more). This provides a method completely internal to JWST to identify any possible AGN interlopers that might be contributing too much at rest 8 μm to give valid SFR estimates.

JWST data can also address the issue of whether to apply the local calibration for centrally concentrated ULIRGs, or whether to apply the calibration for more extended star formation that is dominant at high redshift. It is unlikely that there is an abrupt transition between the two cases. Instead, there is probably a mixture of behaviors with the proportion of centrally concentrated cases decreasing with increasing redshift. This transition appears to be virtually complete by $z = 1$ (Rujopakarn et al. 2013). Below this redshift, JWST photometry can help select the appropriate template through comparing the behavior of the output of the PAH bands, which are dominant for 6–13 μm, with that of the dust grains that dominate the emission at 13–30 μm. For example, the MIRI photometric bands at 12.8 and 21 μm sample these two spectral components separately for $0 < z < 0.6$. Their relative behavior can be expressed by the ratio of the flux densities in the two bands, i.e., $f(21 \, \mu m)/f(12.8 \, \mu m)$. To test the behavior of this ratio, we used the $\log L_{IR}/L_{\odot} = 11.25$ and $\log L_{IR}/L_{\odot} = 12.25$ templates from Rieke et al. (2009); the former is representative of the SEDs of high-redshift ULIRGs, while the latter is for low-redshift ones (Rujopakarn et al. 2012). We found that the ratio (high redshift over low redshift) is a factor of 1.5 or more greater for the low-redshift ULIRG template than for the high-redshift case. This approach can be extended to $z \sim 1$ by using the 15 and 25.5 μm bands in an analogous manner. Although the sensitivity of the latter band is reduced by the thermal emission of the telescope, an integration time of only an hour would provide sufficient signal-to-noise ratio (S/N > 20) for $z = 1$ LIRGs. Below the LIRG luminosity range, the evolution in IR SEDs is no longer a significant issue in estimating SFRs.

7. CONCLUSIONS

We have studied a sample of 105 star-forming galaxies covering a range of total IR luminosity, $L_{IR} = L(8-1000 \, \mu m) = 10^9 - 10^{12} \, L_{\odot}$ and redshift $0 < z < 0.4$ to calibrate the luminosity of the PAH features at 6.2−11.3 μm as SFR indicators. The total PAH luminosity (6.2 μm + 7.7 μm + 11.3 μm features) correlates linearly with the SFR as measured by the extinction-corrected Hα luminosity (using the sum of the observed Hα emission and corresponding 24 μm luminosity as established by Kennicutt et al. 2009), with a tight scatter of 0.14 dex. The scatter is similar to those seen in comparing other accurate indicators of SFRs, showing that the PAH-derived values are also accurate.

---

[15] We select these bands because they start at the wavelength of the channel 1 IRAC band and are spaced by about a factor of 1.5 in wavelength.

We have provided a new robust SFR calibration using the luminosity emitted from the PAHs at 6.2, 7.7, and 11.3 μm and all possible combinations. The scatter is smallest, $\sigma_{MAD} = 0.14$ dex (i.e., 40%), whenever the 7.7 μm feature is involved in the fit. This implies that this feature may provide the most robust measure of the SFR. The relation against the 6.2 μm feature has the highest scatter, $\sigma_{MAD} = 0.21$ dex (i.e., 60%), which may indicate more variation in galaxies between the luminosity in this feature and the SFR. For low-redshift galaxies ($z < 0.5$), this calibration is valid only up to the high LIRG/ULIRG luminosity range, where IR luminosities at and above this range underestimate the SFR. We have also demonstrated that in the case of star-forming galaxies, the rest-frame broadband 7.7 μm emission should also be a robust SFR tracer, if samples of AGNs can be excluded.

The PAH SFR calibration shows a dependency on galaxy gas-phase metallicity, where the PAH luminosity of galaxies with $Z \lesssim 0.7\, Z_\odot$ departs from the linear SFR relationship. We have calibrated a correction to the PAH SFRs using a simple empirical model that depends linearly on metallicity for a sample of 25 galaxies. Larger samples of low-metallicity galaxies are necessary to improve the accuracy of these fits on the dependence of gas-phase metallicity and reduce the scatter seen in the metallicity relations.

We have presented a case study for observations from *JWST* that will be capable of measuring the PAH luminosities in galaxies to $z \lesssim 2$. Because the PAH features are so bright, our PAH SFR calibration enables an efficient way to measure SFRs in distant galaxies with *JWST* to SFRs as low as ~10 $M_\odot$ yr^{-1} for galaxies that dominate the peak of the SFR density evolution. We used *Spitzer*/IRS observations of PAH features in seven lensed star-forming galaxies at $1 < z < 3$ to demonstrate the utility of the PAHs to derive SFRs as accurate as those available from other indicators. We demonstrate that the SFRs from the PAHs are consistent with those derived from Hα+24 μm (and from Paα when it is available).

The PAH features may provide the most accurate SFR measurements for distant galaxies, $z \lesssim 2$, with *JWST*/MIRI spectroscopy and photometry with much higher S/N than other SFR indicators. This is because the PAH luminosities are brighter than most other SFR indicators (Paα and Brα) with S/N higher by factors >5–10 in comparable exposure times. For this reason, the PAH features will be the brightest SFR indicators in high-redshift galaxies, and the calibration we provide will have a large utility for studies with *JWST* of galaxies in the distant universe. This new SFR indicator will be useful for probing the peak of the SFR density in the universe ($z \lesssim 2$), and because PAHs trace star formation even in galaxies with AGNs, this new SFR indicator allows for studies of the co-evolution of star formation and supermassive blackhole accretion contemporaneously in a galaxy.

REFERENCES

Allam, S. S., Tucker, D. L., Lin, H., et al. 2007, ApJL, 662, L51
Alonso-Herrero, A., Ramos Almeida, C., Esquej, P., et al. 2014, MNRAS, 443, 2766
Asplund, M., Grevesse, N., Sauval, A. J., & Scott, P. 2009, ARA&A, 47, 481
Battisti, A. J., Calzetti, D., Johnson, B. D., & Elbaz, D. 2015, ApJ, 800, 143
Beers, T. C., Flynn, K., & Gebhardt, K. 1990, AJ, 100, 32
Bendo, G. J., Draine, B. T., Engelbracht, C. W., et al. 2008, MNRAS, 389, 629
Berta, S., Lutz, D., Santini, P., et al. 2013, A&A, 551, A100
Brandl, B. R., Bernard-Salas, J., Spoon, H. W. W., et al. 2006, ApJ, 653, 1129
Brinchmann, J., Charlot, S., White, S. D. M., et al. 2004, MNRAS, 351, 1151
Brown, M. J. I., Moustakas, J., Smith, J.-D. T., et al. 2014, ApJS, 212, 18
Calzetti, D., Kennicutt, R. C., Engelbracht, C. W., et al. 2007, ApJ, 666, 870
Chabrier, G. 2003, PASP, 115, 763
Chary, R., & Elbaz, D. 2001, ApJ, 556, 562
Dey, A., Jannuzi, B. T., Brown, M. J. I., et al. 2004, BAAS, 36, 746
Diamond-Stanic, A. M., & Rieke, G. H. 2010, ApJ, 724, 140
Diamond-Stanic, A. M., & Rieke, G. H. 2012, ApJ, 746, 168
Donley, J. L., Koekemoer, A. M., Brusa, M., et al. 2012, ApJ, 748, 142
Donley, J. L., Rieke, G. H., Pérez-González, P. G., & Barro, G. 2008, ApJ, 687, 111
Elbaz, D., Dickinson, M., Hwang, H. S., et al. 2011, A&A, 533, A119
Elbaz, D., Hwang, H. S., Magnelli, B., et al. 2010, A&A, 518, L29
Engelbracht, C. W., Gordon, K. D., Rieke, G. H., et al. 2005, ApJL, 628, L29

Farrah, D., Bernard-Salas, J., Spoon, H. W. W., et al. 2007, ApJ, 667, 149
Finkelstein, K. D., Papovich, C., Finkelstein, S. L., et al. 2011, ApJ, 742, 108
Finkelstein, S. L., Papovich, C., Rudnick, G., et al. 2009, ApJ, 700, 376
Fiolet, N., Omont, A., Lagache, G., et al. 2010, A&A, 524, A33
Fu, H., & Stockton, A. 2009, ApJ, 696, 1693
Fumagalli, M., Labbé, I., Patel, S. G., et al. 2014, ApJ, 796, 35
Goldader, J. D., Goldader, D. L., Joseph, R. D., Doyon, R., & Sanders, D. B. 1997, AJ, 113, 1569
Haan, S., Armus, L., Surace, J. A., et al. 2013, MNRAS, 434, 1264
Hainline, K. N., Shapley, A. E., Kornei, K. A., et al. 2009, ApJ, 701, 52
Hernán-Caballero, A., Pérez-Fournon, I., Hatziminaoglou, E., et al. 2009, MNRAS, 395, 1695
Ho, L. C. 2005, ApJ, 629, 680
Ho, L. C., & Keto, E. 2007, ApJ, 658, 314
Hwang, H. S., Elbaz, D., Magdis, G., et al. 2010, MNRAS, 409, 75
Inami, H., Armus, L., Surace, J. A., et al. 2010, AJ, 140, 63
Jannuzi, B. T., & Dey, A. 1999, in ASP Conf. Ser. 191, Photometric Redshifts and the Detection of High Redshift Galaxies, ed. R. Weymann et al. (San Francisco, CA: ASP), 111
Jannuzi, B. T., Dey, A., Brown, M. J. I., et al. 2004, BAAS, 36, 1478
Kauffmann, G., Heckman, T. M., Tremonti, C., et al. 2003, MNRAS, 346, 1055
Kennicutt, R. C., Jr. 1998, ARA&A, 36, 189
Kennicutt, R. C., Jr., Calzetti, D., Walter, F., et al. 2007, ApJ, 671, 333
Kennicutt, R. C., & Evans, N. J. 2012, ARA&A, 50, 531
Kennicutt, R. C., Jr., Hao, C.-N., Calzetti, D., et al. 2009, ApJ, 703, 1672
Kewley, L. J., Dopita, M. A., Sutherland, R. S., Heisler, C. A., & Trevena, J. 2001, ApJ, 556, 121
Kirkpatrick, A., Pope, A., Alexander, D. M., et al. 2012, ApJ, 759, 139
Kochanek, C. S., Eisenstein, D. J., Cool, R. J., et al. 2012, ApJS, 200, 8
Kroupa, P., & Weidner, C. 2003, ApJ, 598, 1076
Lacy, M., Petric, A. O., Sajina, A., et al. 2007, AJ, 133, 186
Lacy, M., Storrie-Lombardi, L. J., Sajina, A., et al. 2004, ApJS, 154, 166
Le Floc'h, E., Papovich, C., Dole, H., et al. 2005, ApJ, 632, 169
Lin, H., Buckley-Geer, E., Allam, S. S., et al. 2009, ApJ, 699, 1242
Lutz, D. 2014, ARA&A, 52, 373
Lutz, D., Sturm, E., Tacconi, L. J., et al. 2008, ApJ, 684, 853
Madau, P., & Dickinson, M. 2014, ARA&A, 52, 415
Magnelli, B., Elbaz, D., Chary, R. R., et al. 2009, A&A, 496, 57
Marcillac, D., Rieke, G. H., Papovich, C., et al. 2008, ApJ, 675, 1156

Menéndez-Delmestre, K., Blain, A. W., Smail, I., et al. 2009, ApJ, 699, 667
Moustakas, J., & Kennicutt, R. C., Jr. 2006, ApJS, 164, 81
Moustakas, J., Kennicutt, R. C., Jr., Tremonti, C. A., et al. 2010, ApJS, 190, 233
Moustakas, J., Zaritsky, D., Brown, M., et al. 2011, arXiv:1112.3300
Murphy, E. J., Chary, R.-R., Dickinson, M., et al. 2011, ApJ, 732, 126
Muzzin, A., van Dokkum, P., Kriek, M., et al. 2010, ApJ, 725, 742
O'Dowd, M. J., Schiminovich, D., Johnson, B. D., et al. 2009, ApJ, 705, 885
Osterbrock, D. E. 1989, Astrophysics of Gaseous Nebulae and Active Galactic Nuclei (Mill Valley, CA: Univ. Science Books), 84
Papovich, C., Rudnick, G., Rigby, J. R., et al. 2009, ApJ, 704, 1506
Pereira-Santaella, M., Diamond-Stanic, A. M., Alonso-Herrero, A., & Rieke, G. H. 2010, ApJ, 725, 2270
Pérez-González, P. G., Rieke, G. H., Egami, E., et al. 2005, ApJ, 630, 82
Pettini, M., & Pagel, B. E. J. 2004, MNRAS, 348, L59
Pope, A., Chary, R.-R., Alexander, D. M., et al. 2008, ApJ, 675, 1171
Pope, A., Wagg, J., Frayer, D., et al. 2013, ApJ, 772, 92
Rieke, G. H., Alonso-Herrero, A., Weiner, B. J., et al. 2009, ApJ, 692, 556
Rigby, J. R., Marcillac, D., Egami, E., et al. 2008, ApJ, 675, 262
Rosario, D. J., Trakhtenbrot, B., Lutz, D., et al. 2013, A&A, 560, A72
Rujopakarn, W., Rieke, G. H., Eisenstein, D. J., & Juneau, S. 2011, ApJ, 726, 93
Rujopakarn, W., Rieke, G. H., Papovich, C. J., et al. 2012, ApJ, 755, 168
Rujopakarn, W., Rieke, G. H., Weiner, B. J., et al. 2013, ApJ, 767, 73
Sargsyan, L. A., & Weedman, D. W. 2009, ApJ, 701, 1398
Seitz, S., Saglia, R. P., Bender, R., et al. 1998, MNRAS, 298, 945
Shi, Y., Rieke, G. H., Ogle, P., Jiang, L., & Diamond-Stanic, A. M. 2009, ApJ, 703, 1107
Shipley, H. V., Papovich, C., Rieke, G. H., et al. 2013, ApJ, 769, 75
Smail, I., Smith, G. P., & Ivison, R. J. 2005, ApJ, 631, 121
Smith, J. D. T., Draine, B. T., Dale, D. A., et al. 2007, ApJ, 656, 770
Stern, D., Eisenhardt, P., Gorjian, V., et al. 2005, ApJ, 631, 163
Teplitz, H. I., Chary, R., Elbaz, D., et al. 2011, AJ, 141, 1
Teplitz, H. I., McLean, I. S., Becklin, E. E., et al. 2000, ApJL, 533, L65
Tremonti, C. A., Heckman, T. M., Kauffmann, G., et al. 2004, ApJ, 613, 898
Treyer, M., Schiminovich, D., Johnson, B. D., et al. 2010, ApJ, 719, 1191
Wu, Y., Helou, G., Armus, L., et al. 2010, ApJ, 723, 895
Wuyts, E., Rigby, J. R., Gladders, M. D., et al. 2012, ApJ, 745, 86
Xu, L., Rieke, G. H., Egami, E., et al. 2015, ApJS, 219, 18
Yuan, F.-T., Takeuchi, T. T., Buat, V., et al. 2011, PASJ, 63, 1207